



HAL
open science

Evolution of a Shallow Volcanic Arc Pluton During Arc Migration: A Tectono-Thermal Integrated Study of the St. Martin Granodiorites (Northern Lesser Antilles)

Mélanie Noury, Mélody Philippon, Jean-Jacques Cornee, Matthias Bernet, Olivier Bruguier, Leny Montheil, Lucie Legendre, Elza Dugamin, Michael Bonno, Philippe Münch

► To cite this version:

Mélanie Noury, Mélody Philippon, Jean-Jacques Cornee, Matthias Bernet, Olivier Bruguier, et al.. Evolution of a Shallow Volcanic Arc Pluton During Arc Migration: A Tectono-Thermal Integrated Study of the St. Martin Granodiorites (Northern Lesser Antilles). *Geochemistry, Geophysics, Geosystems*, 2021, 22, 10.1029/2020GC009627 . insu-03594271

HAL Id: insu-03594271

<https://insu.hal.science/insu-03594271>

Submitted on 2 Mar 2022

HAL is a multi-disciplinary open access archive for the deposit and dissemination of scientific research documents, whether they are published or not. The documents may come from teaching and research institutions in France or abroad, or from public or private research centers.

L'archive ouverte pluridisciplinaire **HAL**, est destinée au dépôt et à la diffusion de documents scientifiques de niveau recherche, publiés ou non, émanant des établissements d'enseignement et de recherche français ou étrangers, des laboratoires publics ou privés.



Distributed under a Creative Commons Attribution - NonCommercial - NoDerivatives 4.0 International License

Geochemistry, Geophysics, Geosystems®



RESEARCH ARTICLE

10.1029/2020GC009627

Special Section:

A fresh look at the Caribbean plate geosystems

Key Points:

- The tectono-thermal history of the St. Martin Oligocene granodiorite is reconstructed
- Exhumation occurred during two periods: between 27 and 24 Ma and since 9 Ma, along N45° trending normal faults
- Regionally, exhumation rates suggest a southward migration of the deformation associated with the opening of the Anegada Trough

Supporting Information:

Supporting Information may be found in the online version of this article.

Correspondence to:

M. Noury,
mnoury@geologia.unam.mx

Citation:

Noury, M., Philippon, M., Cornée, J.-J., Bernet, M., Bruguier, O., Montheil, L., et al. (2021). Evolution of a shallow volcanic arc pluton during arc migration: A tectono-thermal integrated study of the St. Martin granodiorites (northern Lesser Antilles). *Geochemistry, Geophysics, Geosystems*, 22, e2020GC009627. <https://doi.org/10.1029/2020GC009627>

Received 11 JAN 2021
Accepted 13 NOV 2021

Author Contributions:

Conceptualization: Mélody Philippon, Philippe Münch

Data curation: Mélody Philippon, Matthias Bernet, Olivier Bruguier, Michael Bonno

Formal analysis: Mélody Philippon

© 2021. The Authors.

This is an open access article under the terms of the [Creative Commons Attribution-NonCommercial-NoDerivs License](https://creativecommons.org/licenses/by-nc-nd/4.0/), which permits use and distribution in any medium, provided the original work is properly cited, the use is non-commercial and no modifications or adaptations are made.

Evolution of a Shallow Volcanic Arc Pluton During Arc Migration: A Tectono-Thermal Integrated Study of the St. Martin Granodiorites (Northern Lesser Antilles)

Mélanie Noury^{1,2} , Mélody Philippon² , Jean-Jacques Cornée² , Matthias Bernet³, Olivier Bruguier⁴ , Leny Montheil⁴ , Lucie Legendre² , Elza Dugamin^{2,5}, Michael Bonno⁴, and Philippe Münch⁴ 

¹Estación Regional del Noroeste, Instituto de Geología, Universidad Nacional Autónoma de México, Hermosillo, México, ²Géosciences Montpellier, CNRS-Université de Montpellier-Université des Antilles, Campus de Fouillole, Montpellier, France, ³Université Grenoble-Alpes, CNRS, ISTERre (Institut des Sciences de la Terre), Grenoble, France, ⁴Géosciences Montpellier, CNRS-Université de Montpellier-Université des Antilles, Montpellier, France, ⁵Université de Lorraine, CNRS, Nancy, France

Abstract A new data set combining thermobarometry, geo-thermochronology, chronostratigraphic, and structural analyses highlights the tectono-thermal evolution of the St. Martin granodiorite from its emplacement to its surface exposure. The described vertical motions in this part of the upper plate of the Lesser Antilles subduction zone since 30 Myrs are linked to the migration of the Lesser Antilles volcanic arc toward the plate interior. Results suggest that the St. Martin granodioritic pluton emplaced at 4–5 km depth and underwent a four-step history: (a) 30–27 Ma, emplacement along N20–40° transtensive structures oblique to the trench followed by, (b) 27–24 Ma, rapid post-emplacement cooling and exhumation (~0.6 mm/yr) controlled by perpendicular to the trench N45° trending structures, (c) 24–9 Ma, slow subsidence (0.01 mm/yr) and development of carbonate platforms associated to tectonic quiescence, westward migration of the arc, and subsequent cooling of the crust, (d) 9 Ma to present-day, exhumation (~0.25 mm/yr) and uplift of Neogene carbonate platforms mainly along N45° faults that likely accommodate the progressive trench curvature since 30 Ma. Pecube forward modeling using this scenario reproduces both the observed present-day geometry and thermochronometric ages. A similar sequence of events is observed in the Virgin Islands. Along with our new data, this suggests a southward migration of the deformation associated with the opening of the Anegada Trough.

1. Introduction

Along subduction trenches, strain partitioning, vertical motions (of both rocks and surface), and volcanic activity respond to variations in large-scale slab dynamics while accommodating global geodynamical changes (e.g., Cailleau & Oncken, 2008; Corrigan et al., 1990; Geist et al., 1993; Gvirtzman & Nur, 1999; Heuret et al., 2007; Martinod et al., 2016; Yáñez & Cembrano, 2004). Consequently, subducting margins have been for decades a natural laboratory for geoscientists to better understand the interplay between upper crustal processes and deep and/or large-scale processes along subduction zones. Here, we focus on the vertical motions and strain changes associated with the migration of a volcanic arc toward the plate interior. Processes originating these changes are still debated, but may include: (a) tectonic erosion following the subduction of asperities scraping off/eroding the upper plate that can ultimately lead to forearc subduction (e.g., Clift & Vannucchi, 2004; Keppie et al., 2009; Lallemand et al., 1992), (b) slab flattening following the subduction of a buoyant anomaly belonging to the down-going plate (e.g., Espurt et al., 2007; Martinod et al., 2010; van Hunen et al., 2002), or (c) a relative change in the plate motion with the upper plate pushing the trench toward the subducting plate interior (e.g., van Hunen et al., 2000). The migration of the volcanic arc is accommodated by forearc strain and vertical motion, which can be upward (surface and/or rock uplift) or downward (surface and/or rock subsidence) (Lallemand et al., 1992; Martinod et al., 2020; Noury et al., 2017).

Multi-method low-temperature thermochronology combined with zircon U-Pb dating is a powerful tool to elucidate the thermal and temporal evolution of volcanic arcs. Along subducting margins, it provides insights on the timing of island-arc growth and unroofing. For example, along the Hikurangi margin (New Zealand) thermochronometry allowed determining rapid phases of magmatic thickening and burial (lasting 6 Myrs) followed

Funding acquisition: Mélody Philippon, Philippe Münch

Investigation: Mélody Philippon, Jean-Jacques Cornée, Matthias Bernet, Olivier Bruguier, Lény Montheil, Lucie Legendre, Elza Dugamin, Michael Bonno, Philippe Münch

Methodology: Mélody Philippon

Project Administration: Mélody Philippon, Philippe Münch

Resources: Mélody Philippon, Jean-Jacques Cornée, Matthias Bernet, Olivier Bruguier, Lény Montheil, Lucie Legendre, Elza Dugamin, Philippe Münch

Supervision: Jean-Jacques Cornée, Matthias Bernet, Philippe Münch

Validation: Jean-Jacques Cornée, Matthias Bernet, Olivier Bruguier, Michael Bonno, Philippe Münch

Visualization: Mélody Philippon

Writing – original draft: Mélody Philippon, Philippe Münch

Writing – review & editing: Mélody Philippon, Jean-Jacques Cornée, Matthias Bernet, Olivier Bruguier, Lény Montheil

by contrasting slow unroofing (lasting 40 Myrs) (e.g., Flowers et al., 2005). Along many volcanic arcs it has been demonstrated that active volcanoes were emplaced in their own metamorphosed magmatic basement that was promptly exhumed (Kuril: De Grave et al., 2016; Lesser Antilles: Favier et al., 2019). It is noteworthy that during arc migration, cooling of an arc pluton might be interpreted to record its exhumation, whereas it might be associated with a drop in the paleo-geothermal gradient due to volcanic arc cessation (Kohút & Danišík, 2017). However, the effects on thermochronological ages of the evolution through time of the thermal structure of the crust can be investigated using a numerical modeling approach.

In order to shed light on the behavior of upper plate subduction zones during arc migration, an integrated study of the St. Martin granodiorite has been conducted. This Oligocene volcanic arc pluton is exposed in the present-day forearc of the Lesser Antilles arc on St. Martin island. To characterize the pressure-temperature-time (P-T-t) path of the granodiorite pluton we performed *in situ* thermobarometry using Al composition of fresh hornblendes coupled with several isotopic dating techniques covering a wide range of closure temperatures (T_c): zircon U-Pb dating (T_c superior to temperature of crystallization), $^{40}\text{Ar}/^{39}\text{Ar}$ dating of amphiboles ($T_c \sim 535 \pm 65^\circ\text{C}$, Harrison, 1982) and biotites ($T_c \sim 330 \pm 50^\circ\text{C}$, Grove & Harrison, 1996), zircon and apatite fission-track dating ($T_c \sim 225 \pm 35^\circ\text{C}$, Brandon et al., 1998 and $T_c \sim 110 \pm 30^\circ\text{C}$, Ketcham et al., 1999, respectively), as well as (U-Th)/He dating of apatite ($T_c \sim 50 \pm 30^\circ\text{C}$, Farley, 2000). We then modeled the thermal history of the pluton using the QTQt program (Gallagher, 2012). We coupled this P-T-t data set with a thorough analysis of the geology and paleostress and used the Pecube software (Braun, 2003) to perform forward models investigating the role of tectonics in the observed age pattern. Finally, we discuss the exhumation history of the pluton and place it in a regional geodynamical context.

2. Geological Settings

2.1. Regional Geodynamical Evolution

The Lesser Antilles arc emplaced during middle Eocene along the eastern margin of the Caribbean plate following a major kinematic change of the North American Plate (Figure 1). Following the arc initiation on the Anguilla bank, the magmatic arc that was in St. Barthélemy (40–17 Ma) and St. Martin (57–28 Ma) shifted westward, toward the plate interior, and settled at its present-day location in the Saba and St. Kitts and Nevis islands (400 Kyr - present day) (Bouysse et al., 1990; Briden et al., 1979; Dagain et al., 1989; Defant et al., 2001; Legendre et al., 2018; Nagle et al., 1976). The subduction of an aseismic ridge is believed to have flattened the slab, triggering a 10 Ma gap in the volcanic activity and its westward migration (Bouysse et al., 1990). However, it has been established that the oceanic ridges did not exist during the Paleogene and that the volcanic activity might have been continuous over this period (Pichot et al., 2012). Indeed, new geochronometric data suggest a slow westward arc migration through time (Legendre et al., 2018). Because of intraplate deformation, and contemporaneously with the migration of the volcanic arc, the northern Lesser Antilles forearc was segmented into deep V-shaped basins and highs (Boucard et al., 2021). These highs expose various crustal levels of the Eocene-lowermost Miocene arc: from its roots intruding Eocene marine deposits in St. Martin and St. Barthélemy, to its surface deposits in Antigua (e.g., Andréieff et al., 1988; Cornée et al., 2020; Legendre et al., 2018; Westercamp & Andréieff, 1983). To the north, the Anguilla bank is bounded by the Anegada Trough, a transtensive deep basin trending parallel to the V-Shaped basins, which crosscuts the Lesser Antillean forearc. These N40° trending structures are thought to accommodate strain in the upper plate since the late Oligocene-early Miocene (Boucard et al., 2021; Chaytor & ten Brink, 2015; Jany et al., 1990; Laurencin et al., 2017).

2.2. Geology of St. Martin

St. Martin island is located in the Lesser Antillean forearc and is characterized by ~2,000–3,000 m thick interbedded Eocene volcanoclastic rocks (57–55 Ma to 40 Ma, Dagain et al., 1989), lava flows and carbonate rocks dipping ~30° toward the SSE (Dagain et al., 1989, Figure 2). These rocks are intruded by two calc-alkaline plutonic bodies (Figure 2; Andréieff et al., 1988; Briden et al., 1979; Christman, 1953; Nagle et al., 1976) of tonalite to granodiorite composition, both having the same texture and petrology and sharing a similar chemical evolution, and thus belonging to the same magmatic series (Dagain et al., 1989; Davidson et al., 1993). The granodiorite has been dated at ~30 Ma (whole rock K-Ar dating; Briden et al., 1979; Nagle et al., 1976, Figure 2). The intrusion is believed to have caused extensive contact metamorphism in the Eocene volcano-sedimentary host-rocks, at least

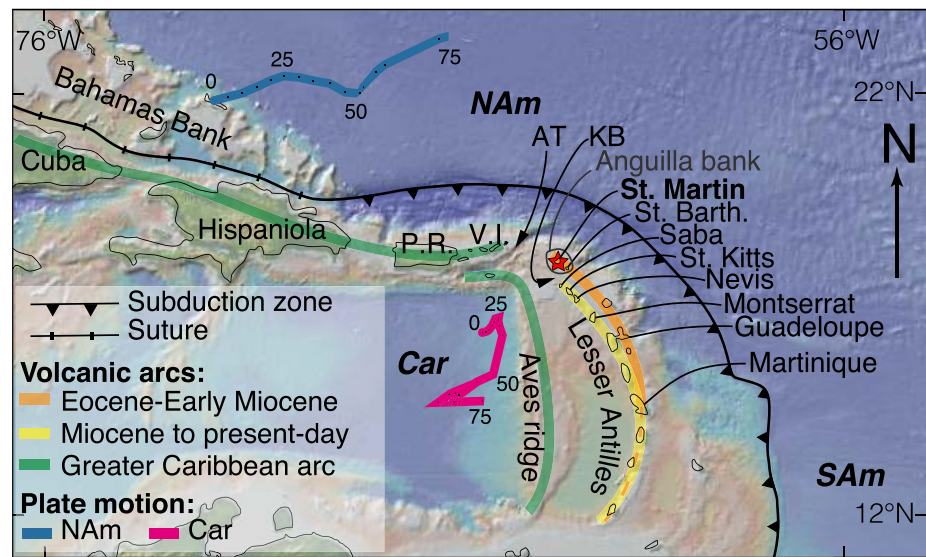


Figure 1. Geodynamical map of the eastern edge of the Caribbean Plate. The red star indicates the location of St. Martin island. The present-day location of the Greater Caribbean arc across the Greater Antilles and the Aves ridge is shown in green. The Eocene-Early Miocene and Miocene to present-day Lesser Antilles volcanic arcs are indicated by orange and yellow thick lines, respectively. In the northern Lesser Antilles, these two arc are separated by the Kalinago Basin (KB). NA, SA and Car stands for North American, South American and Caribbean plates, respectively. Caribbean and North American plate motions are represented by thick blue and pink lines, respectively. These motions are depicted in the hotspot reference frame (Dobrovine et al., 2012) and ages of the major kinematic changes are indicated by numbers. AT indicates the localization of the Anegada Trough, a large transtensive structure formed north of the Lesser Antilles during the early Miocene.

at the scale of the island (Bonneton & Vila, 1983; Dagain et al., 1989; Davidson et al., 1993). A 26.1 ± 4 Ma whole rock K-Ar age obtained for an andesite within the Eocene series by Nagle et al. (1976) and recalculated by Briden et al. (1979) was thus attributed to reflect contact metamorphism during intrusion of the pluton by Andréieff et al. (1988) (Figure 2). The Eocene series and the Oligocene plutonic bodies are unconformably overlain by a tabular ~250 m thick lower to upper Miocene carbonate platform.

St. Martin shows four normal fault directions: $N20^{\circ}$ – $N40^{\circ}$, N–S and their conjugated $N120^{\circ}$ – 145° and E–W faults (Dagain et al., 1989). The granodiorite emplaced along $N20^{\circ}$ – $N40^{\circ}$ trending faults and E–W trending faults deformed both the intrusion and the country rock (Dagain et al., 1989). The observed SE dipping of the Eocene and Oligocene units must relate to a pre-Miocene tilting event as the Miocene carbonate platform is tabular (Andréieff et al., 1988; Dagain et al., 1989); it has been attributed to a pre-Oligocene regional tilting (Andréieff et al., 1988; Dagain et al., 1989; Westercamp & Andréieff, 1983).

3. Methods

In this study, we use zircon U-Pb, hornblende and biotite $^{40}\text{Ar}/^{39}\text{Ar}$, apatite and zircon fission-track and apatite (U-Th)/He dating to quantify the exhumation history of the Northern Lesser Antilles forearc on St. Martin island. For this purpose, several kilograms of rocks were sampled in the field: one sample (SM16-25) was collected from an andesite located 1 km away from the pluton and intercalated within the lower Eocene series, two samples (SM15-02 and SM15-17) were collected from the plutonic body located in the south of the island, and four samples in its northern part (samples SM15-07, SM15-09, SM15-18 and SM15-21; Figure 2). Part of the samples was used to make thin-sections for microprobe analysis and the remaining sample material was crushed and sieved for mineral separation. Using standard magnetic and heavy liquid separation techniques, amphibole, biotite, apatite and zircon were extracted and analyzed as described in the Sections 3.2–3.5. To extract the thermal histories from the geo-thermochronological data, inverse time-temperature modeling approaches were used. A structural data set acquired over 224 sites across the island and consisting in ~1,000 measurements of bedding, fractures, faults, and kinematics criteria is presented. It allows to characterize the paleo stress field before, during and after

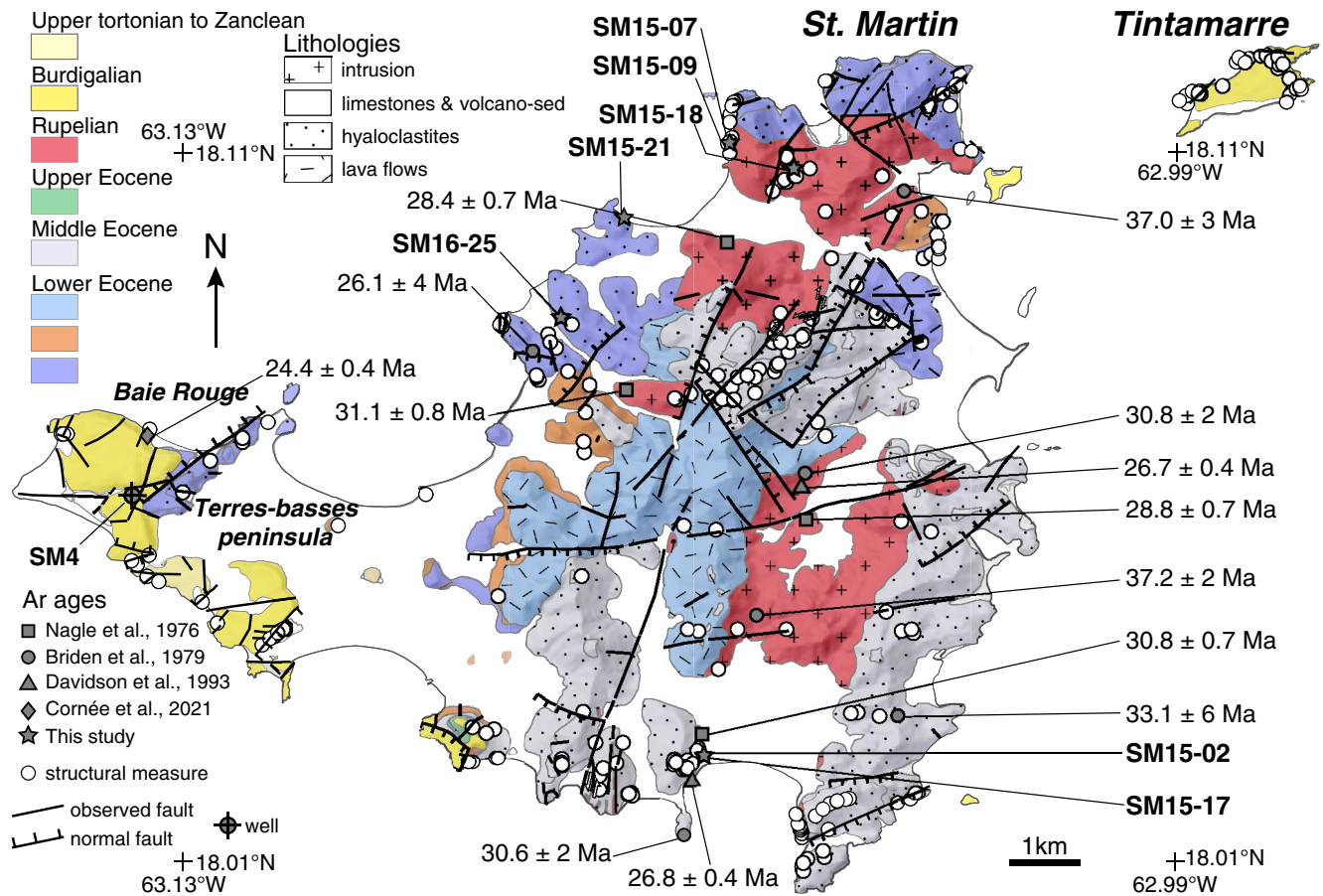


Figure 2. Simplified geological map of St. Martin after Dagain et al., 1989. Previously published K-Ar ages by Nagle et al. (1976), Briden et al. (1979) and $^{40}\text{Ar}/^{39}\text{Ar}$ ages by Davidson et al. (1993) and Cornée et al. (2021) are indicated. Gray stars indicate samples locations presented in this study. White dots indicate the localization of structural measurements (beddings and/or faults).

the emplacement of the granodiorite. Finally, a series of NW–SE sections allows us to reconstruct the timing of tilting versus the timing of the intrusion.

3.1. Amphibole Thermobarometry

Amphibole thermobarometry has been widely used to estimate emplacement depths and crystallization temperature of igneous rocks in different geodynamical settings (e.g., Ague & Brimhall, 1988; Anderson et al., 1988; Sisson et al., 1989). In this study, we applied the method proposed by Mutch et al. (2016) that is calibrated for low-pressure granitic rocks. Polished rock thin-sections were carbon-coated and major element compositions of amphibole and plagioclase were determined using a CAMECA SX-100 electron microprobe equipped with five wavelength-dispersive X-ray spectrometers (WDS) at the *Service Microsonde Sud (Université Montpellier II)*. All analyses were performed using 20 keV accelerating voltage, a focused beam of 10 nA and a counting time of 20–30s. Pure metals, synthetic oxides and natural minerals were used as standards and concentrations were obtained from raw intensities using the “X-PHI” quantification procedure (Merlet, 1994).

As recommended by Mutch et al. (2016), analyses were performed in rocks containing the mineral assemblage: amphibole + plagioclase + biotite + quartz + alkali feldspar + magnetite + apatite + Ti-oxide. Analyses were performed on amphiboles and plagioclase rims in apparent textural equilibrium with the rest of the mineral assemblage. Composition of the plagioclase allowed to determine the crystallization temperature (Holland & Blundy, 1994). For all analyzed samples, the crystallization temperature is close to the haplogranite solidus

($725 \pm 75^\circ\text{C}$) and thus allowed the calculation of the pressure of crystallization of adjacent hornblendes with the barometer developed by Mutch et al. (2016). Raw thermobarometrical data are available in the supplementary materials (Table S1 in Supporting Information S1).

3.2. Zircon U-Pb Dating

A fraction of the zircons was mounted in epoxy, polished and used to perform conventional zircon U-Pb dating. We analyzed *ca.* 25 grains using the laser ablation inductively coupled plasma mass-spectrometry (LA-ICP-MS) system at the University of Montpellier II (AETE-ISO regional facility of the OSU OREME, CNRS-INSU) using a single collector Element XR ICP-MS (ThermoFisher) and a 193 nm Compex 102 laser (Lambda Physik). The operating conditions and data acquisition were as described in Bosch et al. (2011). Laser spot sizes of 50 μm with a 15 J/cm^2 energy density at a repetition rate of 4 Hz were used. Analyte signals were acquired during 45 s with a blank measured during 15 s for each sample. The 91500 zircon standard (Wiedenbeck et al., 1995) was used for external standardization of Pb/Pb and U-Pb ratios measured on unknown minerals. Raw data of the zircon U-Pb analyses are available online in the Geochron data repository (see data availability statement section).

3.3. $^{40}\text{Ar}/^{39}\text{Ar}$ Dating

For granodiorite samples, fresh hornblende and biotite crystals were handpicked under a stereo microscope from the 100–200 μm -size fraction of crushed samples. For the andesite, a 200–300 μm -size fraction of fresh mesostase was separated and handpicked. Crystals and the mesostase were subsequently leached with HNO_3 (1N) for a few minutes and then repeatedly cleaned ultrasonically in distilled water and alcohol in order to remove alteration products prior to being packed in aluminum foil. All samples were encapsulated for irradiation at the Triga Mark II nuclear reactor at Pavia (Italy) along with several aliquots of the Taylor Creek sanidine standard (28.305 ± 0.036 Ma; Renne et al., 1998) as flux monitors. The argon isotopic interferences on K and Ca were determined by the irradiation of KF and CaF_2 pure salts from which the following correction factors were obtained: ($^{40}\text{Ar}/^{39}\text{Ar}$) $K = 0.00969 \pm 0.00038$, ($^{38}\text{Ar}/^{39}\text{Ar}$) $K = 0.01297 \pm 0.00045$, ($^{39}\text{Ar}/^{37}\text{Ar}$) $\text{Ca} = 0.0007474 \pm 0.000021$, and ($^{36}\text{Ar}/^{37}\text{Ar}$) $\text{Ca} = 0.000288 \pm 0.000016$.

The gas extraction and purification lines consist of (a) an IRCO2 laser of 100 kHz used at 3%–20% power to heat the samples during 60 s, (b) a lens system for beam focusing, (c) a steel chamber, maintained at 10^{-8} – 10^{-9} bar, with a copper holder in which 2-mm-diameter blind holes were milled, and (d) two Zr-Al getters for the purification of the gases. The argon isotopes were analyzed with a multicollector mass spectrometer (Argus VI from Thermo-Fisher). The mass discrimination was monitored daily using an automated air pipette and provided a mean value of 0.99985 ± 0.00274 per dalton. Blank analyses were performed after every three sample analyses. Raw data of each step and blank were processed and ages were calculated using the ArArCALC-software (Koppers, 2002). The criteria for defining plateau ages are: (a) plateau steps should contain at least 70% of released ^{39}Ar , (b) there should be at least three successive steps in the plateau and (c) the integrated age of the plateau should agree with each apparent age of the plateau within a 2σ confidence interval. Uncertainties are at the 2σ level, including the error on the irradiation factor. Data and results of the $^{40}\text{Ar}/^{39}\text{Ar}$ analyses are available online in the Geochron data repository (see data availability statement section).

3.4. Zircon and Apatite Fission-Track Dating

Around one hundred zircon and apatite grains from each sample were handpicked from the 100–200 μm -size fraction obtained after conventional mineral separation methods (sieving, magnetic separation, density separation using heavy liquids) (e.g., Kohn et al., 2019). Crystals of zircon and apatite were then embedded in Teflon® sheets and epoxy resin, respectively. Samples were then prepared for fission-track dating with the external detector method (Fleischer et al., 1964; Naeser & Dodge, 1969). All grain mounts were then polished to expose internal crystal surfaces. In order to reveal spontaneous fission-tracks, zircons were etched in a NaOH–KOH melt at 228°C for several hours (Bernet et al., 2004; Tagami et al., 1990) and apatites were etched with a 5.5 N HNO_3 solution at 21°C for 20 s (Carlson et al., 1999). Apatite and zircon grain mounts were covered with uranium-poor muscovite sheets as external detectors and irradiated at the FRM II reactor in Garching, Germany. Apatite samples were irradiated with a nominal fluence of 4.5×10^{15} n/cm^2 along with Fish Canyon Tuff and Durango apatite age standards and with IRMM540R (15 ppm) dosimeter glasses. Zircon samples were irradiated

with a nominal fluence of 0.5×10^{15} n/cm² along with Fish Canyon Tuff age standards and IRMM541 (50 ppm) dosimeter glasses. After irradiation, the muscovite detectors of all mounts were etched for 18 min in 48% HF at 21°C to reveal induced tracks. Fission-tracks in apatite and zircon mounts and mica detector were counted dry at 1,250x magnification using an Olympus BX51 microscope and the FTStage 4.04 system (Dumitru, 1993) at the ISTerre fission-track laboratory of the Geo-Thermochronology platform at the Université Grenoble Alpes, France. We used the same system to measure horizontally confined tracks-in-track lengths. Only crystals with well-polished surfaces, mounted parallel to the c-axis, not showing mineral inclusions or strong track-density zoning were analyzed. Raw data of the fission-track analyses are available online in the Geochron data repository (see data availability statement section).

3.5. Apatite (U-Th)/He Dating

The (U-Th)/He analyses were performed at *Géosciences Montpellier* (France), following the method described in Wu et al. (2016). Apatite grains were hand-picked from the 100–200 μm size fraction to select euhedral specimens free of inclusions and fractures. All aliquots consist of a single grain and were heated at ~900°C for 12 min with a 1,090 nm fiber laser operating at 20W. This heating allowed extracting ~99.9% of the total amount of ⁴He in the grains as shown by replicate heating. Gas purification was achieved with a cryogenic trap and two SAES AP-10-N getters and helium was measured with a Quadrupole PrismaPlus QMG 220. After He extraction, U and Th were measured using isotope dilution ICP-MS on the same aliquots after dissolution in 220 ml of doubly spiked (²³⁰Th, ²³³U) HNO₃ 13 N at 120°C for 2 hr. Apatite helium ages were calculated and corrected for α emission following the procedure of Gautheron et al. (2009). Durango apatite replicates were analyzed each three analyzed samples. During the course of this study, we obtained an age of 30.9 ± 0.6 Ma (2σ) for the Durango apatite standard which is in good agreement with the Durango apatite (U-Th)/He age of 31.13 ± 1.01 Ma reported by McDowell et al. (2005). In the text, we report central ages calculated from individual grain ages with the Radial Plotter software (Vermeesch, 2009). Raw data obtained for the (U-Th)/He analyses are available online in the Geochron data repository (see data availability statement section).

3.6. Thermal History Modeling

3.6.1. Cooling History Modeling Inverting Thermochronological Data (QTQt)

The apatite fission-track annealing and (U-Th)/He diffusion parameters data may be inverted numerically to reconstruct the thermal history of rocks. Here, we used the QTQt approach (Gallagher, 2012; Gallagher et al., 2009) that consists in choosing a set of kinetic parameters and a random cooling history for which predicted data are calculated as well as their probability to fit the observed data. To model our apatite (U-Th)/He data we used the recoil damage model of Gautheron et al. (2009) and the multi-kinetic annealing model of Ketcham et al. (2007) for apatite fission-track ages and track-length distributions. We used a present-day surface temperature of 27.5 ± 7.5 °C as indicated by the MERRA-2 database (Gelaro et al., 2017). For all samples, we used the available zircon U-Pb and ⁴⁰Ar/³⁹Ar ages as constraints on the thermal history; these constraints are discussed in Section 5.3. We used as inputs our zircon and apatite fission-track ages and apatite horizontally confined track length data projected on the c-axis, the D_{par} value as a kinetic parameter, and the annealing model of Ketcham et al. (2007) and Tagami et al. (1998) for apatite and zircon, respectively. Input files used to perform QTQt inversions are provided in the Supporting Information S1. 500,000 t-T paths were tested and confronted to the analytical data set. From the different t-T paths tested, QTQt calculates an expected model, which corresponds to a weighted mean of the different credible t-T paths, the weighting being provided by the posterior probability for each tested path.

3.6.2. Testing a Possible Exhumation History (Pecube Forward Modeling)

In order to test our tectono-magmatic scenario against the obtained thermochronological data, forward Pecube modeling (Braun, 2003) was conducted. Pecube is a finite-element code that solves the heat-transfer equation in three dimensions taking into account the effects of various parameters such as the heat advection by faults, heat production by pluton(s) and the effect of the topography on isotherms at depth (Braun, 2003; Braun et al., 2006). For each node at the surface of the model at the end of the run, Pecube computes the corresponding time-temperature path and associated predicted thermochronometric ages. One of the aims was to check if it is possible to reproduce the observed ages and tilting at the island scale, using a tectonic scenario compatible with our structural analyses.

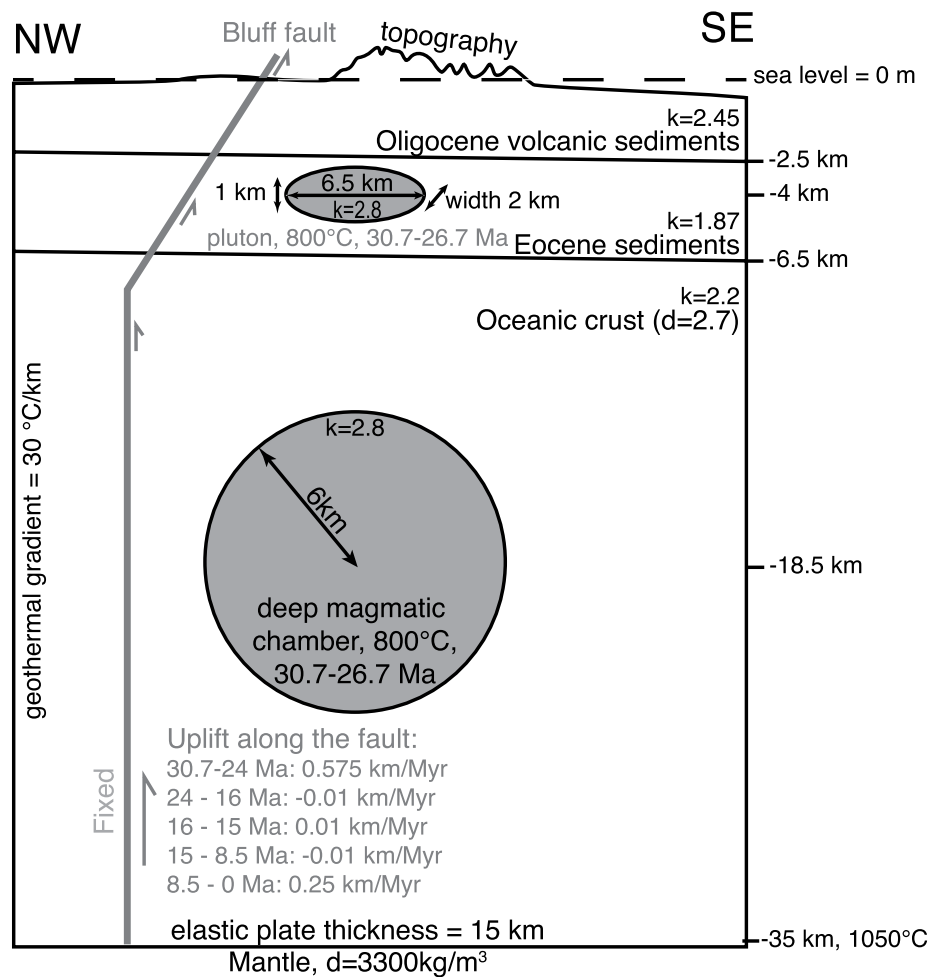


Figure 3. Pecube model initial settings (cross-section perpendicular to the Bluff fault) based on the present-day architecture of the crust in Montserrat island. Magmatic chambers produce heat during the 30.7–26.7 Ma period. Thermal conductivity k used for each lithology is indicated. Four-step tectonic scenario is indicated. We use the DEM of St. Martin island amplified by a 1.5 factor as initial (30.7 Ma) topography. The shallow magmatic chamber greater axis is orientated N–S, as suggested by the present-day extension of the outcropping Oligocene granodiorites.

A modified version of the Pecube-v3.0 code (modified files are provided in the Supporting Information S1) was used to take into account the heat produced by the pluton between ~ 30.7 and ~ 26.7 Ma (ages are defined based on the higher and lower bounds of zircon U–Pb ages) and the thermal diffusivity of the different rocks. Thermal diffusivity was defined as dependent on the thermal conductivity of rocks and temperature using the equations of Vosteen and Schellschmidt (2003). Isostatic rebound was computed for each time step using an elastic plate thickness of 15 km (Jiménez-Díaz et al., 2014) and densities of 2.7 and 3.3 for the crust and mantle, respectively. A $30^\circ\text{C}/\text{km}$ background geothermal gradient was set. The kinetic parameters of Gautheron et al. (2009), Ketcham et al. (2007), Tagami et al. (1998) and Harrison (1982), were used to predict the apatite (U–Th)/He, apatite and zircon fission-track and the hornblende $^{40}\text{Ar}/^{39}\text{Ar}$ ages, respectively.

For the initial time-step, the present-day topography of St. Martin was used amplified by a 1.5 factor, which reproduces a relief similar to the active volcanic arc. For each following time-step, each altitude value making up the initial topography decreases proportionally through time to reach the present-day St. Martin topography at 0 Ma. Surface temperature is defined at sea-level and above at 27.5°C with an atmospheric lapse rate of $5^\circ\text{C}/\text{km}$; below sea level, we used the temperature profile for tropical ocean.

Because Montserrat is a good present-day analog of the St. Martin island in the Oligocene (see Section 6.2.2), we used the crustal structure described for this island to define the initial parameters of our model (Figure 3).

The model has a 35 km crustal thickness (based on the reconstructions by Philippon et al., 2020) and is mainly composed of gabbros with a thermal conductivity of $2.2 \text{ W}\cdot\text{m}^{-1}\cdot\text{K}^{-1}$ (Eppelbaum et al., 2014). It is intruded by a spheric pluton of 6 km radius emplaced at 18.5 km-depth in the center of the model, which corresponds to the mid-crustal magmatic chamber (Paulatto et al., 2012). This magmatic chamber feeds a shallow ellipsoidal magmatic chamber ($6.5 \times 2 \times 1 \text{ km}$; Figure 3) whose center is at 4 km depth below sea-level (Paulatto et al., 2012). We defined the magmatic chambers as composed of granodioritic rocks with thermal conductivity of $2.8 \text{ W}\cdot\text{m}^{-1}\cdot\text{K}^{-1}$ (Eppelbaum et al., 2014). The small pluton intrudes a 4 km pile of sediments of Eocene age (Dagain et al., 1989) with a thermal conductivity of $1.87 \text{ W}\cdot\text{m}^{-1}\cdot\text{K}^{-1}$ (Eppelbaum et al., 2014), which conforms the base of the volcanic edifice, and is in turn capped by volcanoclastic sediments of Oligocene age (water saturated volcanoclastic sandstones and limestones with a thermal conductivity of $2.45 \text{ W}\cdot\text{m}^{-1}\cdot\text{K}^{-1}$; Eppelbaum et al., 2014) whose base stands at 2.5 km below sea level (Paulatto et al., 2010, Figure 3).

3.7. Paleo Stress Tensors

The right dihedral method was employed using the WinTensor software to inverse fault kinematics and obtain the paleo-stress tensor (Angelier, 1979; Angelier & Mechler, 1977; Delvaux & Sperner, 2003). WinTensor allows the rotational optimization of the obtained tensor by performing iterative tests of tensors in order to minimize a misfit function (Delvaux & Sperner, 2003). These inversions were performed on a data set consisting of fault strike, dip, plunge of striae and kinematics criteria. For consistency, a minimum of four structural measurements (faults direction and dip, pitch and kinematics) is needed to obtain a robust paleotensor. The maximum age of faults has been deduced from their structural relationships to the intrusions and the sedimentary series whose ages are well known. Based on these deductions, we grouped the structural data and performed the inversion for five key periods of time: (a) before intrusion of the granodiorite (Late Eocene), (b) syn-intrusion (Rupelian), (c) post-intrusion and ante-Miocene deposition (Aquitainian), (d) syn-deposition of Mio-Pliocene platform deposits (Burdigalian–Zanclean), and (e) post-deposition (post-Zanclean).

4. New Geological and Tectonic Constraints on St. Martin Island

The new structural data set confirms that the Eocene volcanosedimentary series is folded into a monocline trending $\text{N}45^\circ$ and dipping 25° toward the SE (Figure 4). It also demonstrates that the dip of the Eocene series increases at the vicinity of some intrusions and faults (Figure 4). Moreover, various small-scale faults offset the Eocene volcanosedimentary series by several meters. Based on these observations, we estimate a total thickness of max. 1 km for the Eocene series cropping out in St. Martin (Figure 4), unlike previous studies that indicated a total thickness of 3 km (Dagain et al., 1989). Moreover, we obtained a mini-plateau age of $27.8 \pm 0.9 \text{ Ma}$ (Figure 5) for an andesite interbedded in the lower Eocene series (sample SM16-25) in the vicinity of the northern granodiorite. Even if the uncertainties on individual steps are large in relation with high atmospheric argon content, we consider this age as acceptable as the mini-plateau, the inverse isochrone and the total fusion ages are concordant (Figure 5). The age of this andesite is similar to the age of the Oligocene pluton and likely indicate that the dated rock is rather a hypabyssal sill than an interbedded volcanic rock in the Eocene series. Field relationships between the Oligocene intrusion and its country rock suggest that the intrusive body emplaced parallel or sub parallel to the bedding (at least SE of the island) and sometimes along faults cross-cutting the middle Eocene volcano-sedimentary deposits (Figures 6a and 6a').

Chronostratigraphic constraints on the Miocene to early Pliocene carbonate deposits indicate that the outcropping sequence is only *ca.* 50 meters thick on most of the island except for its westernmost portion, where 252 meters of Miocene sediments have been drilled in the well SM4 (Figure 4, Andréieff et al., 1988; Cornée et al., 2021). The oldest deposits found (Mullet pound bay) contain the planktonic foraminifera *Paragloborotalia nana* and *Globigerinoides subquadratus*, indicating a late Aquitainian to early Burdigalian age (21–18 Ma; Cornée et al., 2021).

Consequently, both uplift and erosion of the metamorphosed series occurred prior to the Burdigalian. At Baie Rouge, in the hanging wall of the Bluff fault, unmetamorphosed submarine volcanoclastic deposits crop out between the Eocene and the Burdigalian deposits, above an erosional surface (Figure 4). These deposits were recently dated by Cornée et al. (2021) at 24 Ma, confirming the view of Dagain et al. (1989) who interpreted them as the volcanic counterparts of the Oligocene St. Martin granodiorite. This suggests that erosion is probably older than 24 Ma (latest Oligocene), like in the neighboring island of St. Barthélemy (Cornée et al., 2020), and that

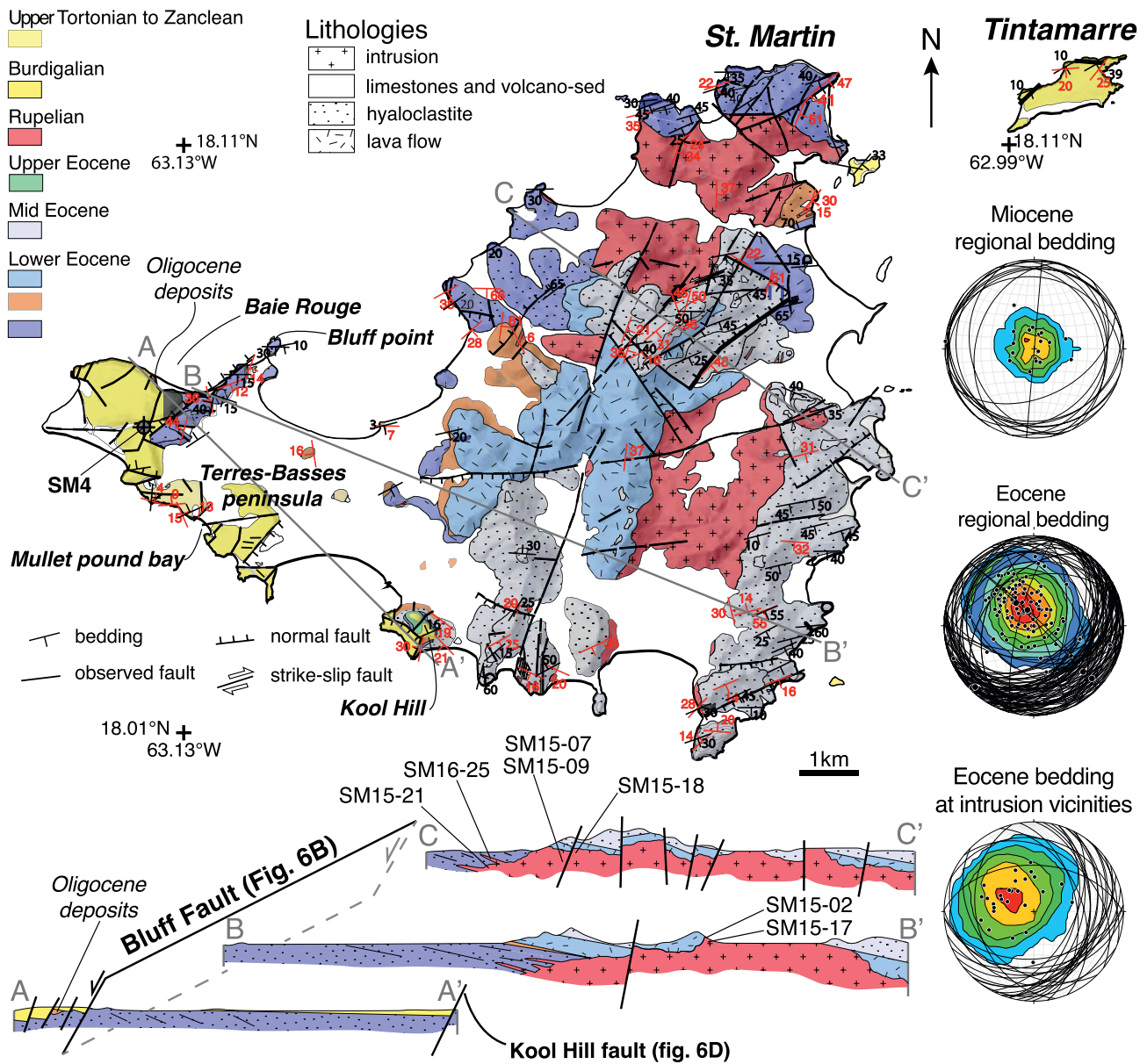


Figure 4. New structural map and cross-sections of St. Martin granodiorite. Stereograms show the Miocene regional bedding (sub-tabular), the Eocene bedding at the intrusion vicinity (reported in red on the map) and the Eocene regional bedding (trending NNE–SSW with a mean dip of 40°). The main structure, the Bluff fault, crops out east of the Terres-Basses peninsula. SM4 indicates the PENARROYA well (1971–72) in which 252.30 m of Miocene sediments have been retrieved.

Oligocene deposits are preserved in the hanging wall of the Bluff normal fault (Figure 4). Noticeable are two other subaerial unconformities: above the Burdigalian deposits where the middle Miocene deposits are missing, and at the top of the series where erosional surfaces are found within Zanclean littoral deposits (Cornée et al., 2021).

4.1. Strain and Paleostress Evolution of the Island

4.1.1. Pre-Intrusion Stress Field

The Eocene series is cross cut by four normal to transpressive fault systems with directions N–S, N30°, N80° and N100° (Figure 7). Only one outcrop exposes a reverse fault offsetting a jasper vein of tens of cm. At the outcrop scale, the paleotensors obtained indicate a NW–SE to NE–SW trending principal axis of stretching with a horizontal σ_3 (Figure 7). Inverting the whole data set together, the resulting paleotensor shows a sub vertical σ_1 (86°

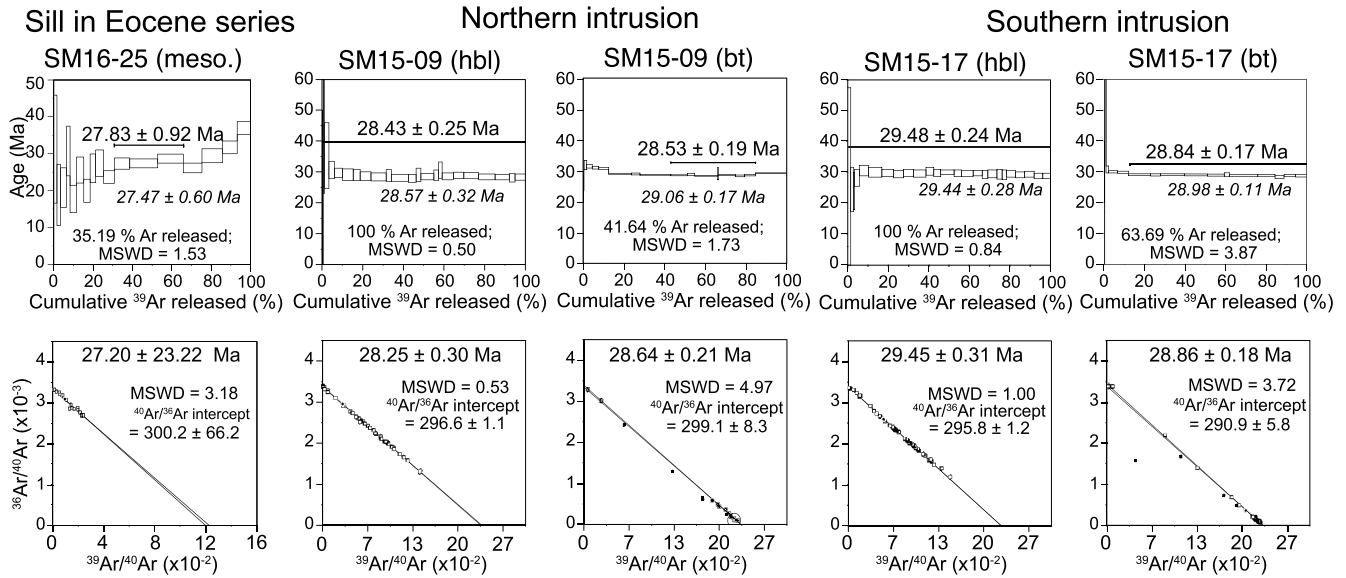


Figure 5. $^{40}\text{Ar}/^{39}\text{Ar}$ spectra (top row) and inverse isochrones (bottom row) for five samples collected in St. Martin: two hornblendes (hbl), two biotites (bt), and an andesite mesostase (meso.). Age plateaus are indicated in the age spectra diagram above a thick line representing the heating steps belonging to the plateau. For each step-heating experiment, total gas age is reported in italics. Ages given by the inverse isochrones and $^{40}\text{Ar}/^{36}\text{Ar}$ intercepts are indicated for each sample in the isochron diagram. MSWD = mean square weighted deviation.

to the N142°), a sub horizontal σ_3 trending N237° with a magnitude similar to σ_2 , indicating a radial extension stress regime during the Late Eocene (Figure 7).

4.1.2. Syn-Intrusion Stress Field

The intrusive bodies emplaced along N–S structures along which we observed transtensive kinematics. At the outcrop scale, σ_3 is sub horizontal and σ_1 plunges from 24° to 69°, defining strike slip to pure extensional stress regimes depending on the fault trend (Figure 7). An inversion of the whole data set shows that σ_1 and σ_3 are sub horizontal (plunging 24° to the N249° and 1° to the N340°, respectively) and that σ_2 is sub vertical (plunging of 63°). The intrusions were thus emplaced in a transtensional stress field with a direction of compression N69° and extension N160° (Figure 7).

4.1.3. Post-Intrusion Stress Fields

The Oligocene granodiorites are crosscut by faults trending N10°, N45° and their conjugated E–W and NW–SE faults. At site scale, σ_3 trends either NW–SE or NE–SW depending on the orientation of the fault. At the scale of the island, the paleo tensor obtained inverting the structural data shows a subvertical σ_1 and sub horizontal σ_2 and σ_3 of similar magnitudes, with σ_3 trending N300°, which indicates a radial extensional stress field for the period of formation of these post-Oligocene (Aquitainian) faults (Figure 7). The Bluff fault (Figure 6b), which belongs to these faults, is sealed by Miocene deposits south of the Terre-Basses peninsula (Figure 7). Its N45° trend is consistent with the SE regional tilt of the whole St. Martin Eo-Oligocene series, which occurred before the deposition of the horizontal Miocene sequence.

We also observed syn-depositional E–W faulting in Burdigalian sediments. For example, at site 43 (Figure 6c), Miocene sediments are affected by E–W normal to slightly transtensive faults that developed under a N–S stress field. At the island scale, inversion of structural data allows to define a paleo tensor with a sub vertical σ_1 and sub horizontal σ_2 and σ_3 of similar magnitudes, σ_3 trending N175° and indicating a radial extension stress field during the deposition of the Burdigalian carbonates (Figure 7).

Finally, we also describe normal faults cross cutting the Miocene sediments and thus formed after the deposition, which ended in the Zanclean. For example, at site 46 in the footwall of the Kool Hill fault (Figure 7), the Miocene sediments unconformably overlie the tilted upper Eocene series, and both formations are offset by a large N45° trending normal fault (Figure 6d). At the scale of the island, an inversion of the data set corresponding to these

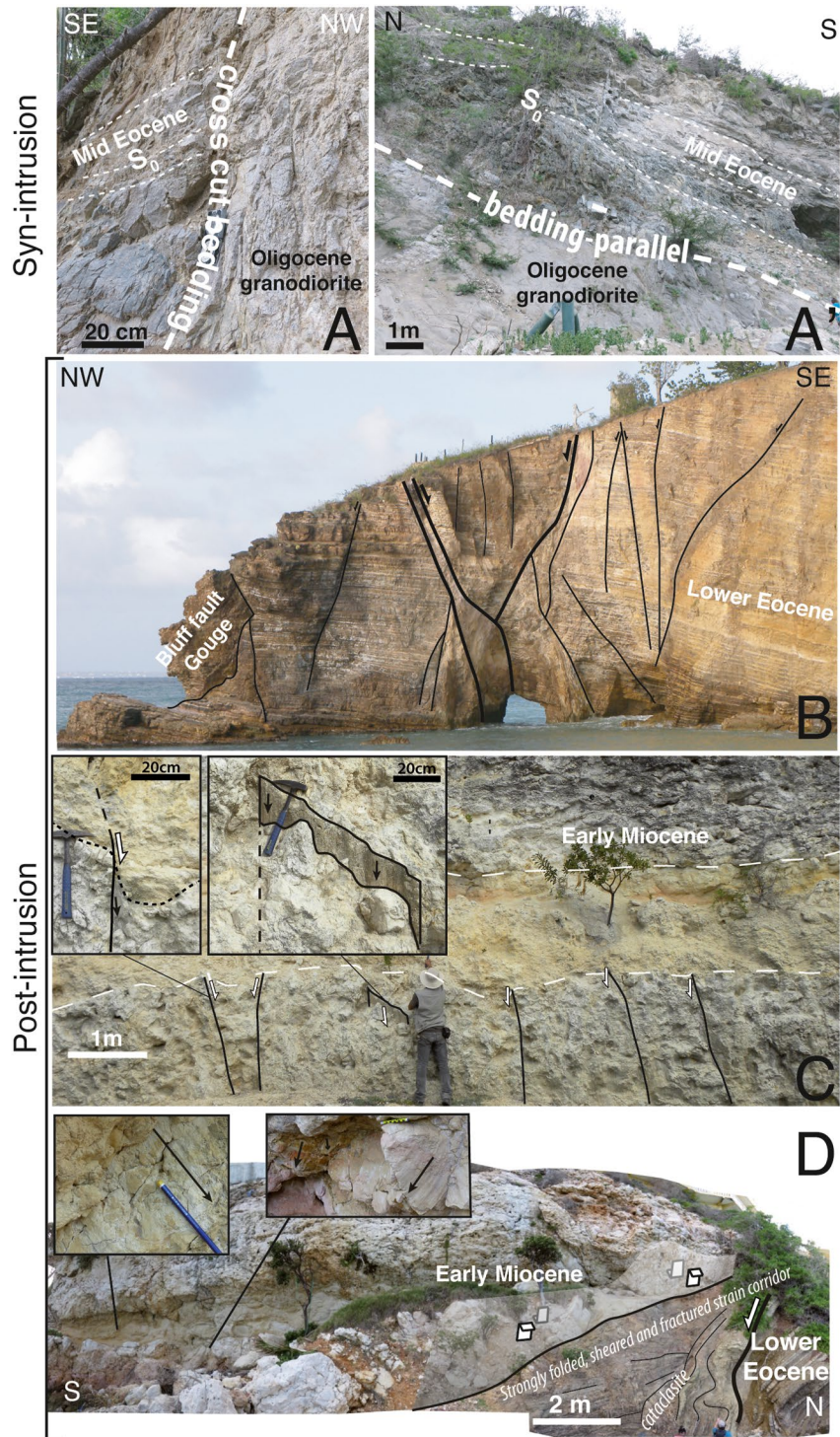


Figure 6. Field photographs of the different structures described in the text (locations of each site are given in Figure 7). (a) and (a') Structural oblique (site 36) and parallel (site 21) relationships between the intrusion and its country rock, respectively. (b) Bluff fault system affecting the ante-intrusion Eocene series (site 40). (c) Burdigalian syn-depositional faulting (site 43). (d) Post-Zanclean N45° trending faulting and local folding of the Eocene series along the Kool Hill fault (site 46).

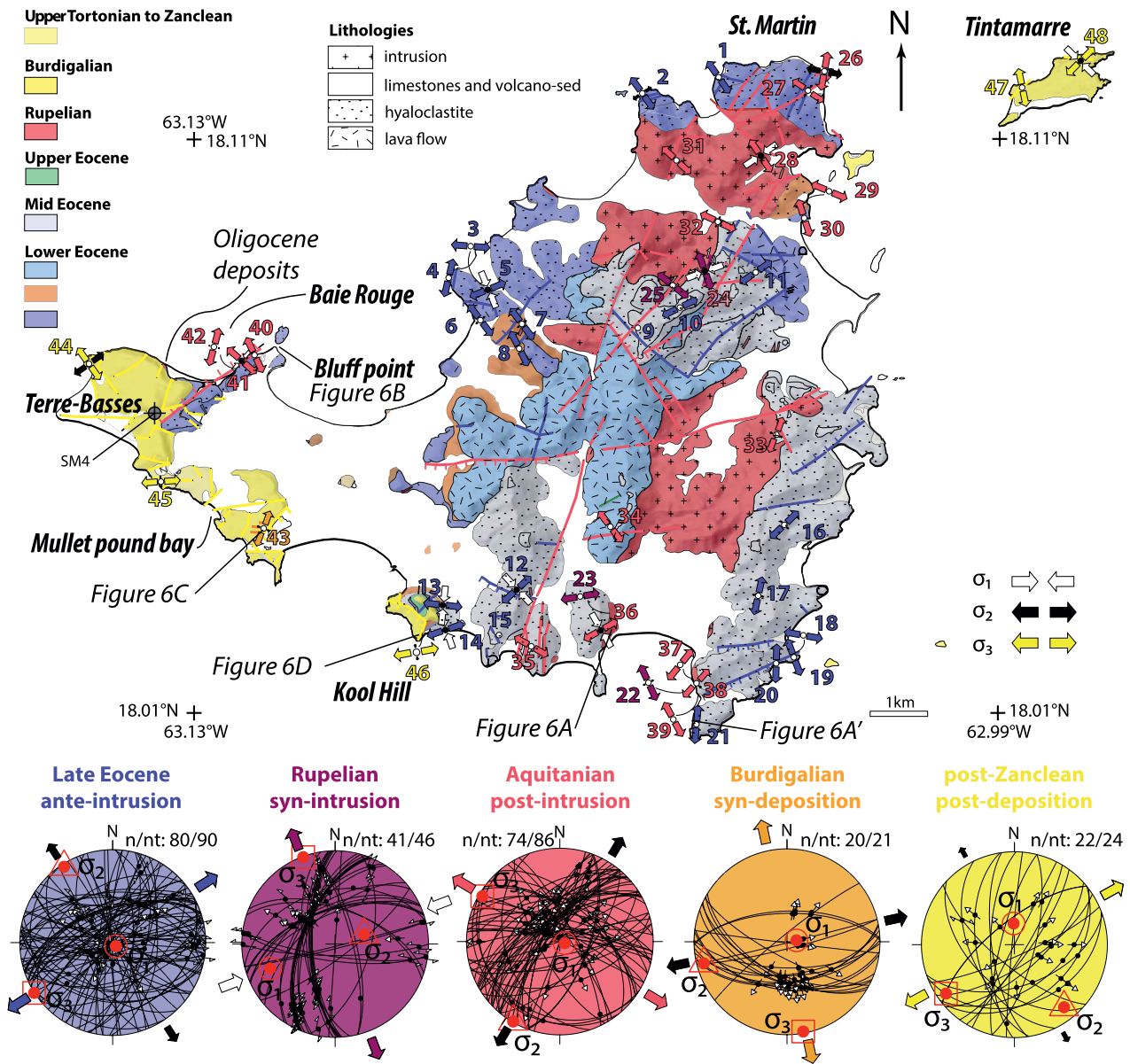


Figure 7. Results of the paleostress inversions as a function time. (a) Schematic map of St. Martin. Faults are colored in function of their period of activity (blue: ante intrusion; purple: syn-intrusion; red: post-intrusion and ante-deposition of the carbonate platform deposits; orange: syn-deposition; yellow: post deposition). On the map, the paleostress tensor of each investigated faults on St. Martin and Tintamarre islands is indicated by colored arrows that show the azimuth of the horizontal stress axes with a length that is proportional to the stress magnitude. The outward or inward black or white arrows indicate compressive and extensive deviatoric stress axes, respectively (Delvaux et al., 1995). (b) Stereonograms showing the paleostress tensor obtained from the field data (faults with kinematic criteria, fractures, and dykes) for each key period identified in this study.

late faults gives a subvertical σ_1 and sub horizontal σ_2 and σ_3 , the latest being trending N240°. These results indicate that the main direction of extension is trending NW–SE since the Zanclean (Figure 7).

5. Depth, Age of Crystallization and Thermal Evolution of the Granodiorite

5.1. Southern Granodiorite

For the southern granodiorite, the analyzed plagioclase–hornblende pairs (sample SM15-02) suggest that this intrusive body emplaced at a depth of 3.75 ± 0.2 km (Table 1). We obtained a zircon U-Pb (crystallization) age of 29.44 ± 0.44 Ma for the same sample (Figure 8). For sample SM15-17 from the same intrusion, we obtained

Table 1
Thermobarometry Results Obtained From the Average Hornblende and Plagioclase Compositions of the Investigated Rocks

Sample	SM15-02		SM15-07		SM15-09		SM15-18	SM15-21	
Specimen	hbl-5	hbl-8	hbl-4	hbl-2	hbl-3	hbl-1	hbl-3	hbl-5	hbl-4
SiO ₂	52.90	52.72	50.86	50.76	50.24	52.57	50.90	50.91	51.58
TiO ₂	0.49	0.64	1.14	1.09	1.19	0.67	0.23	0.90	0.97
Al ₂ O ₃	3.07	3.52	4.53	4.30	5.39	3.95	3.38	3.57	3.59
FeO*	10.74	11.70	10.80	10.55	12.51	11.36	17.48	11.23	10.06
MgO	16.93	16.32	16.33	16.38	15.25	16.40	11.63	15.60	16.85
MnO	0.29	0.35	0.56	0.60	0.33	0.32	0.73	0.32	0.26
CaO	11.62	11.62	11.30	11.12	11.23	11.46	11.74	11.25	11.53
Na ₂ O	0.70	0.97	1.07	0.97	1.26	0.93	0.32	1.07	1.21
K ₂ O	0.25	0.41	0.43	0.41	0.55	0.50	0.11	0.33	0.34
F	0.59	0.89	0.28	0.17	0.60	0.53	0.07	0.28	0.55
Cl	0.19	0.25	0.13	0.11	0.21	0.18	0.05	0.20	0.10
Total	97.77	99.39	97.43	96.46	98.77	98.87	96.64	95.67	97.03
Formula after Holland and Blundy (1994):									
T-sites									
Si	7.58	7.50	7.32	7.36	7.21	7.48	7.59	7.47	7.44
Aliv	0.42	0.50	0.68	0.64	0.79	0.52	0.41	0.53	0.56
Al(total)	0.52	0.59	0.77	0.73	0.91	0.66	0.59	0.62	0.61
M1,2,3 sites									
Alvi	0.10	0.09	0.08	0.09	0.12	0.14	0.19	0.09	0.05
Ti	0.05	0.07	0.12	0.12	0.13	0.07	0.03	0.10	0.11
Fe ³⁺	0.22	0.28	0.34	0.31	0.40	0.25	0.14	0.29	0.29
Mg	3.62	3.46	3.50	3.54	3.26	3.48	2.59	3.41	3.62
Mn	0.04	0.04	0.07	0.07	0.04	0.04	0.09	0.04	0.03
Fe ²⁺	0.98	1.06	0.88	0.87	1.05	1.03	1.96	1.07	0.90
Ca	0.00	0.00	0.00	0.00	0.00	0.00	0.00	0.00	0.00
Sum M1,2,3	5.00	5.00	5.00	5.00	5.00	5.00	5.00	5.00	5.00
M4 site									
Fe	0.09	0.05	0.07	0.10	0.05	0.08	0.08	0.02	0.02
Ca	1.79	1.77	1.74	1.73	1.73	1.75	1.88	1.77	1.78
Na	0.12	0.18	0.18	0.17	0.22	0.18	0.05	0.21	0.19
Sum M4	2.00	2.00	2.00	2.00	2.00	2.00	2.00	2.00	2.00
A site									
Ca	0.00	0.00	0.00	0.00	0.00	0.00	0.00	0.00	0.00
Na	0.07	0.09	0.11	0.10	0.13	0.08	0.05	0.10	0.14
K	0.05	0.07	0.08	0.08	0.10	0.09	0.02	0.06	0.06
Sum A	0.12	0.17	0.19	0.18	0.23	0.17	0.07	0.16	0.21
OH site									
O	0.00	0.00	0.00	0.00	0.00	0.00	0.00	0.00	0.00
OH	1.68	1.54	1.84	1.89	1.67	1.72	1.96	1.82	1.72
F	0.27	0.40	0.13	0.08	0.27	0.24	0.03	0.13	0.25
Cl	0.05	0.06	0.03	0.03	0.05	0.04	0.01	0.05	0.02
Sum OH	2.00	2.00	2.00	2.00	2.00	2.00	2.00	2.00	2.00

Table 1
Continued

Sample	SM15-02		SM15-07		SM15-09		SM15-18	SM15-21	
Specimen	hbl-5	hbl-8	hbl-4	hbl-2	hbl-3	hbl-1	hbl-3	hbl-5	hbl-4
Sum cations	15.12	15.17	15.19	15.18	15.23	15.17	15.07	15.16	15.21
Fe#	0.26	0.29	0.27	0.27	0.32	0.28	0.46	0.29	0.25
Mg#	0.73	0.71	0.72	0.73	0.67	0.71	0.53	0.70	0.74
n	5.00	2.00	5.00	4.00	8.00	6.00	5.00	2.00	6.00
Composition of plagioclase in equilibrium with hornblende:									
XAb	0.81	0.67	0.76	0.75	0.67	0.67	0.62	0.732	0.684
XAn	0.18	0.23	0.21	0.23	0.23	0.23	0.36	0.249	0.300
Thermobarometry:									
T (°C)	668	782	699	711	787	787	682	698	735
P (kbar)	0.94	1.04	1.34	1.28	1.64	1.16	1.05	1.09	1.07
z (km)	3.55	3.94	5.08	4.84	6.18	4.37	3.96	4.10	4.06

Note. XAb and XAn: percentage of albite and anorthite in the analyzed plagioclases, respectively. Temperature T is calculated after Holland and Blundy (1994) thermometry calibration reaction edenite + albite = richterite + anorthite; pressure P is calculated after Mutch et al. (2016). Crystallization depths z are deduced from pressure using a value of 2.7 for the density of the crust. Detailed data are provided in Table S1 in Supporting Information S1.

hornblende and biotite $^{40}\text{Ar}/^{39}\text{Ar}$ plateau ages of 29.48 ± 0.24 and 28.84 ± 0.17 Ma, respectively (Figure 5). This last sample also yielded a 26.3 ± 4.0 Ma zircon fission-track central age (Table 2). The southern granodiorite did not yield apatite, so we did not perform QTQt modeling for these samples. However, we note that all geo-thermochronological ages obtained for this intrusion are equivalent within the 95% confidence interval (Figure 9).

5.2. Northern Granodiorite

In the northern part of the island (samples SM15-07, SM15-09, SM15-18 and SM15-21 – Figure 2), thermobarometry analyses show that hornblende crystallized from 4.0 to 6.2 km-depth (Table 1) between 29.24 ± 1.21 Ma and 27.26 ± 0.35 Ma (zircon U-Pb ages-Figure 8). Zircon fission-track analyses yielded ages between 32.6 ± 4.2 and 29.1 ± 6.0 Ma and are all equivalent within the 2σ error (Table 2). Apatite fission-track ages are more scattered (between 46.5 ± 12.2 and 18.4 ± 2.6 Ma), but are younger or fall within the corresponding zircon fission-track ages considering the 2σ error (Table 2).

For sample SM15-07, we obtained a 27.26 ± 0.35 Ma zircon U-Pb age (Figure 8) and thermobarometry results show that its hornblendes crystallized at ~ 5 km-depth (Table 1; individual values ranging between 4.1 and 5.7 km, Table S1 in Supporting Information S1). In sample SM15-09, we analyzed two hornblendes, one brown (hbl-3) and one green (hbl-1). The first one, hbl-3, is Ti-rich (1.19%) and crystallized at a depth of 6.2 km (Table 1; individual values ranging from 5.2 to 6.7 km, Table S1 in Supporting Information S1), whereas the second one, Ti-poor (0.67%), crystallized at a ~ 4.4 km-depth (Table 1; individual values ranging between 3.4 and 5.6 km, Table S1 in Supporting Information S1). Moreover, the same sample yielded $^{40}\text{Ar}/^{39}\text{Ar}$ plateau ages of 28.4 ± 0.3 and 28.5 ± 0.2 Ma on amphiboles and biotites, respectively (Figure 5). We also performed zircon fission track analyses on sample SM15-09 and obtained a 32.6 ± 4.2 Ma central age.

Samples SM15-07 and SM15-09 both belong to the same granodioritic composite intrusive. These samples were collected close one to the other (~ 150 m) and likely share the same low-temperature history. However, it is noteworthy that zircon U-Pb age obtained for sample SM15-07 is slightly younger (27.26 ± 0.35 Ma) than amphibole and biotite $^{40}\text{Ar}/^{39}\text{Ar}$ ages obtained for sample SM15-09 (28.4 ± 0.3 Ma and 28.5 ± 0.2 Ma, respectively). This may be due to a small difference of crystallization age between the sampled areas of this composite pluton. It is likely that the size of the SM15-07 intrusion was not large enough to reset the $^{40}\text{Ar}/^{39}\text{Ar}$ thermochronometers of sample SM15-09 (located ~ 150 m away from SM15-07). However, these samples have similar apatite fission-track length distributions (negatively skewed distribution with means of 14.54 ± 1.92 and 14.75 ± 1.68 μm , Table 2), which also suggests that they likely shared the same low-temperature history. Therefore, in Table 2, and further in the text, we report as SM15-07 + 09 the data calculated as if apatites from samples SM15-07 and

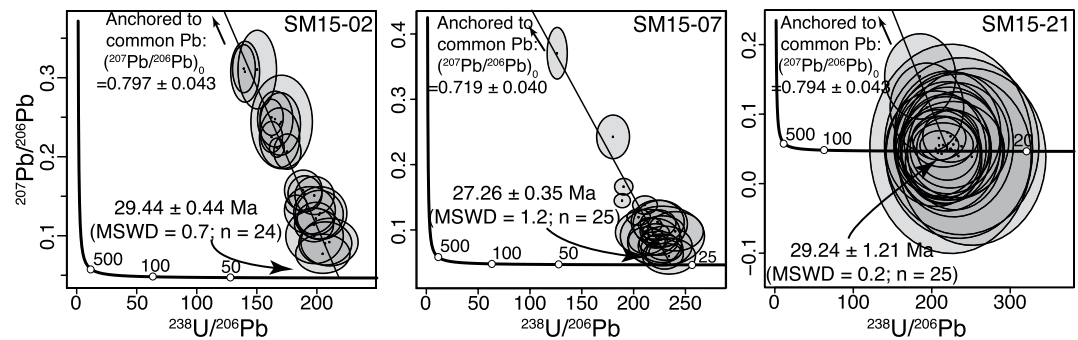


Figure 8. Zircon U-Pb dating results presented as Tera-Wasserburg diagrams for samples from St. Martin intrusives. Lower intercept age and 2σ error are reported. MSWD: mean square weighted deviation, n: number of grains analyzed.

SM15-09 were extracted from the same rock. This allows to calculate a single apatite fission-track central age of 22.6 ± 2.8 Ma for sample SM15-07 + 09. Apatite (U-Th)/He analyses of samples SM15-07 and SM15-09 yielded central ages of 9.5 ± 1.5 and 6.3 ± 0.2 Ma, respectively.

Sample SM15-18 shows an emplacement depth of 4.0 km (Table 1; individual values ranging from 3.1 to 4.4 km, Table S1 in Supporting Information S1). Zircon U-Pb age or intermediate temperature $^{40}\text{Ar}/^{39}\text{Ar}$ analyses were not performed on this sample, but zircon and apatite fission-track ages are equivalent within the 2σ error with central ages of 30.1 ± 2.6 and 35.3 ± 6.0 Ma, respectively (Table 2). Five different apatites gave a central (U-Th)/He age of 20.6 ± 1.3 Ma, with individual ages ranging from 18.07 ± 0.14 to 27.16 ± 0.21 Ma (Table 3).

For sample SM15-21, which corresponds to a granodiorite in contact with the Eocene volcano-sedimentary hosting rock, we obtained a ~ 4.1 km-depth crystallization of hornblendes (Table 1; individual values ranging from 2.7 to 6.5 km, Table S1 in Supporting Information S1) and a 29.24 ± 1.21 zircon U-Pb age (Figure 8). No $^{40}\text{Ar}/^{39}\text{Ar}$ ages were obtained for this granodiorite, but the zircon and apatite fission-track ages are equivalent within the 2σ error with ages of 29.1 ± 6.0 and 46.5 ± 12.2 Ma, respectively (Table 2). Moreover, an apatite

Table 2
Fission Track Analyses Results Obtained With the External Detector Method

Sample	Latitude (°)	Longitude (°)	Min	Elev. (m)	Central age $\pm 2\sigma$ (Ma)	n	Ns	Ni	ρ_s	ρ_i	ρ_d	U (ppm)	P(χ^2)	D	MPTL (μm)
SM15-07	18.11222	-63.05306	A	10	27.8 ± 4.6	20	220	1,396	3.624	22.996	1.238 ± 1.16	27.5	0.22	16	14.54 ± 1.92 (14)
SM15-09	18.11083	-63.05278	A	20	18.4 ± 2.6	22	212	1,982	2.648	24.754	1.242 ± 1.20	30.37	0.46	0	14.75 ± 1.68 (38)
			Z	19	32.6 ± 4.2	18	578	401	8.773	6.087	0.361 ± 1.92	26.39	0.03	20	-
SM15-07 + 09	-	-	A	15	22.6 ± 2.8	42	432	3,378	3.069	23.996	1.238 ± 1.20	29.01	0.03	19	14.61 ± 1.84 (52)
SM15-18	18.10722	-63.04500	A	90	35.3 ± 6.0	16	164	815	2.261	11.237	1.246 ± 1.24	16.05	0.87	0	-
			Z	90	30.1 ± 2.6	20	1,188	894	15.352	11.553	0.362 ± 2.06	60.84	0.37	0	-
SM15-21	18.09972	-63.06694	A	10	46.5 ± 12.2	15	93	351	1.548	5.844	1.258 ± 1.43	6.9	0.19	22	-
			Z	10	29.1 ± 6.0	19	492	372	9.310	7.039	0.363 ± 2.14	32.86	0	32	-
SM15-17	18.02583	-63.05750	Z	45	26.3 ± 4.0	19	469	405	12.654	10.928	0.362 ± 1.99	52.33	0.3	15	-

Note. Apatite age determinations were performed with $\zeta = 277.3 \pm 15.9$ for glass dosimeter IRMM540R and zircon age determinations were performed with $\zeta = 125.5 \pm 6.2$ for glass dosimeter IRMM541 according to protocol defined in text. Min: mineral dated, A and Z stand for apatite and zircon, respectively; n: number of grains counted; N_s and N_i : number of spontaneous and induced fission-track, respectively; ρ_s and ρ_i : mean density of spontaneous and induced tracks (10^5 tracks. cm^{-2}), respectively; ρ_d : effective track density for the fluence monitor (10^6 tracks. cm^{-2}) and associated error (%); U: mean uranium content in analyzed grains (ppm); P(χ^2): probability that the single grain ages represent one population; D: age dispersion (%); MPTL: mean projected track length (number of track-in-track lengths measured is indicated in parenthesis). Detailed data are provided in Supporting Information S1.

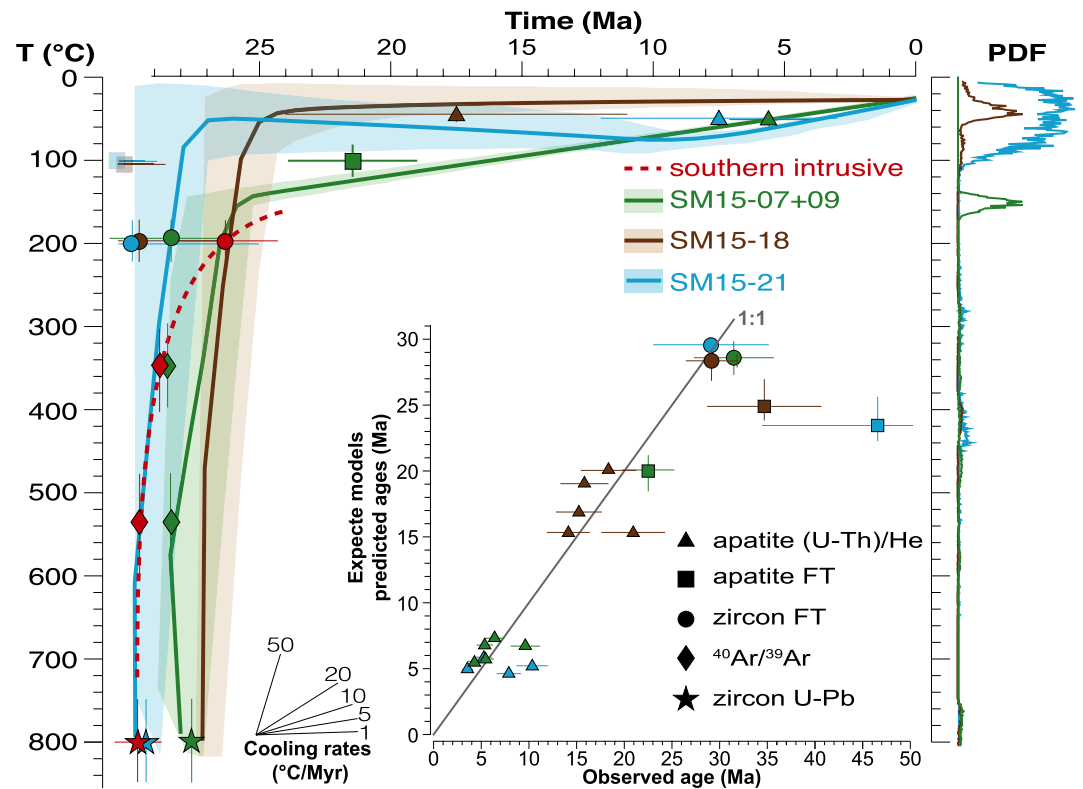


Figure 9. Modeled thermal histories for the samples from the granodioritic intrusions of St. Martin island. Expected models and 95% confidence interval errors obtained for the sample from the northern granodiorite from QTQt (Gallagher, 2012) are represented by a thick line and a colored area, respectively. Samples SM15-07+09, SM15-18 and SM15-21 are represented in green, brown and blue, respectively. Central ages and associated errors obtained by different geo-thermochronological methods and used to perform the inversions are indicated. The probability density function of each expected model for the 28–26 Ma time interval is indicated at right. The predicted versus observed ages plot allows to infer how well each QTQt expected model fits the data. Input QTQt files as well as individual sample modeling results (Figure S1 in Supporting Information S1) are provided as supplementary files.

(U-Th)/He central age of 7.9 ± 1.6 Ma was obtained from the analysis of four individual apatites whose ages are dispersed between 4.64 ± 0.04 and 13.17 ± 0.10 Ma (Table 3).

5.3. Thermal History Modeling of the St. Martin Island

Our geochronological and thermochronological data set allows investigating the thermal history of the northern intrusive of St. Martin island using the QTQt software. There is no direct geological observation such as an unconformity affecting the northern pluton, that could give a constraint on the timing of exposition of the sampled rocks. However, we used our zircon U-Pb ages as initial constraint boxes set at $800 \pm 50^\circ\text{C}$. Moreover, we used the $^{40}\text{Ar}/^{39}\text{Ar}$ ages obtained on hornblendes and biotites (Figure 5) to define constrained boxes at temperatures of $535 \pm 65^\circ\text{C}$ (Harrison, 1982) and $325 \pm 50^\circ\text{C}$ (Grove & Harrison, 1996), respectively. Ages obtained by zircon and apatite fission-track and apatite (U-Th)/He analyses on individual ages as well as fission-track lengths distributions were then inverted using the Markov Chain Monte Carlo approach integrated in QTQt (Gallagher, 2012, Figure 9; raw outputs of QTQt for the expected models are presented in Figure S1 in Supporting Information S1).

Because the emplacement of this plutonic body is shallow (<6km-depth), it is expected to equilibrate with its hosting rocks rapidly after emplacement (<2Myr, Fu et al., 2010; Habert & de Saint-Blanquat, 2004; de Saint-Blanquat et al., 2006). Yet, QTQt allows generating plots of the mean of the probability distribution of the temperature over a selected time range (see QTQt user guide, Gallagher, 2012). In order to better define the temperature uncertainty on the inflection point of the thermal history (that corresponds to the transition between

Table 3
Analytical Data for (U-Th)/He on Apatite Age Determinations

Sample	Grain morphology	4He (nccSTP/g)	$\pm\sigma$ 4He	U (ppm)	Th (ppm)	eU (ppm)	weight (μg)	Width (μm)	Length (μm)	Height (μm)	Rs (μm)	FT Age (Ma)	Corrected Age (Ma)	$\pm\sigma$ (Ma)
SM15-07a2	Abraded hexagonal prism-1 pyramid	21414.1	214.1	15.5596	11.6035	18	7.1	130	102	254	67	0.81	11.94	0.10
SM15-07a7	Tetragonal prism-1 pyramid	8627.5	86.3	5.3110	24.3553	11	11	147	160	192	78	0.85	7.59	0.06
SM15-09a4	Abraded hexagonal prism-1 pyramid	31484.4	314.8	42.8703	73.0096	60	3.6	105	70	SM15-07 central age:	51	0.75	5.77	0.04
SM15-09a5	Hexagonal prism-no pyramid	16734.1	167.3	17.8207	31.1079	25	3.4	116	100	122	53	0.81	6.79	0.05
SM15-09a8	Abraded tetragonal prism-2 broken faces	16178.5	161.8	18.3040	26.8307	25	10	110	163	177	72	0.85	6.39	0.05
SM15-18a1	Tetragonal prism-2 broken faces	20349.4	203.5	6.8035	10.0800	9	18	160	180	190	88	0.89	20.58	0.18
SM15-18a2	Tetragonal prism-2 broken faces	37885.5	378.9	15.5974	28.0733	22	2.8	65	126	SM15-09 central age:	46	0.78	6.3	0.2
SM15-18a3	Hexagonal prism-1 pyramid	55862.4	558.6	17.7734	48.6095	29	7.1	136	120	106	69	0.82	18.07	0.14
SM15-18a5	Tetragonal prism-2 broken faces	97988.4	979.9	32.2987	88.8196	54	5	80	100	222	69	0.82	19.26	0.16
SM15-18a6	Abraded tetragonal prism-no pyramid	54924.4	549.2	14.2515	31.6104	22	6.1	99	110	197	54	0.79	19.25	0.15
SM15-21a2	Hexagonal prism-1 pyramid	46178.5	461.8	15.9466	87.8757	37	6.5	128	120	175	60	0.77	27.16	0.21
SM15-21a3	Hexagonal prism-no pyramid	9975.0	99.8	8.0239	62.4952	23	6.4	133	123	SM15-18 central age:	67	0.79	20.6	1.3
SM15-21a5	Hexagonal prism-no pyramid	8101.3	81.0	4.9721	32.1441	13	12	165	128	220	67	0.79	13.17	0.10
SM15-21a6	Hexagonal prism-2 pyramids	15030.1	150.3	7.1369	35.9823	16	5	110	100	168	65	0.78	4.64	0.04
										230	79	0.86	6.20	0.05
										257	61	0.76	10.46	0.08
										SM15-21 central age:	7.9		7.9	1.6

Note. Detailed data are provided in Supporting Information S1.

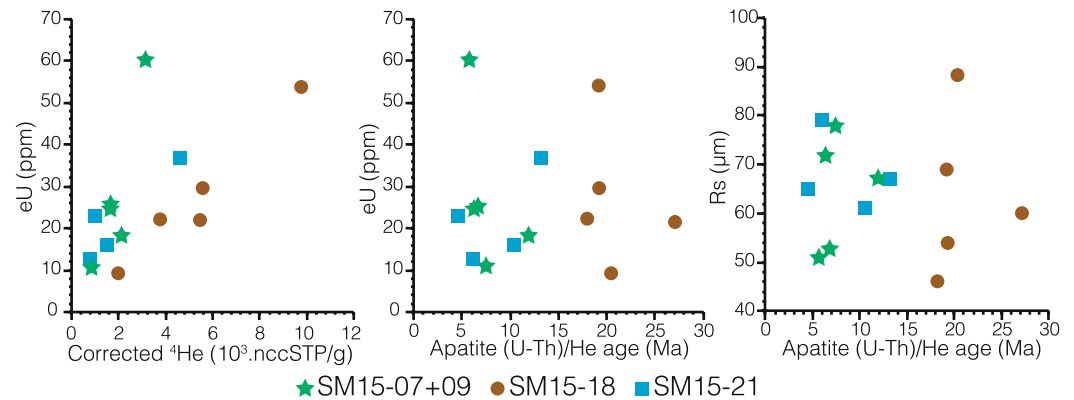


Figure 10. Plots of apatite (U-Th)/He analyses parameters used to assess the origin of the single-grain ages variations inside a sample. eU is the effective uranium content ($eU = U + 0.24 \cdot Th$). Green, brown and blue dots correspond to sample SM15-07+09, SM15-18 and SM15-21, respectively.

the first and second stage of post-intrusion cooling), we present these plots (Figure 9, right panel) for the 2 Myr time range following the last dated pulse of intrusion of the pluton (28–26 Ma).

Similarity among the U-Pb, $^{40}\text{Ar}/^{39}\text{Ar}$ and fission-track ages confirms that both the northern and southern intrusives cooled very rapidly after their emplacement at shallow depth (<6 km, Table 1 and Figure 9). However, expected models for samples from the northern intrusive suggest that after this rapid cooling, time-temperature paths were slightly different. It has to be noted that the obtained expected models for the northern intrusive fit the zircon fission-track ages and the apatite (U-Th)/He ages, as well as the apatite fission-track central age and measured track lengths distribution obtained for sample SM15-07+09 (Figure 9 and Figure S1a in Supporting Information S1). However, apatite fission-track central ages obtained for samples SM15-18 and SM15-21 appear too old to be well reproduced by the models (Figure 9, S1b and and Figure S1c in Supporting Information S1). This may be due to the low number of apatites that could be analyzed in these two samples, which induce large errors on the central ages that, as a result, appear older than the zircon U-Pb and fission-track ages.

Results for sample SM15-07+09 suggest a monotonous cooling from temperatures of $150 \pm 15^\circ\text{C}$ (maximum probability density for the 2 Myr time-range following the emplacement) to $30 \pm 5^\circ\text{C}$ between 26 ± 2 Ma and present-day (Figure 9 and Figure S1a in Supporting Information S1). This corresponds to a cooling rate of $4.7 \pm 1.1^\circ\text{C}/\text{Myr}$. The expected model obtained for sample SM15-18 shows that the maximum probability density for the 28–26 Ma period corresponds to temperatures of $35 \pm 20^\circ\text{C}$ and the present-day temperature is modeled at $25 \pm 5^\circ\text{C}$. These values imply that since at least the lower Miocene sample SM15-18, which is located in the footwall of a post-emplacement normal fault striking NW–SE, was close to or at surface. However, there are no known granodiorite clasts in the Neogene deposits, suggesting that plutons were not exposed before the Zanclean (~4 Ma). Thermal history of sample SM15-21 is more complex. It suggests that this sample, located at the northwestern border of the northern intrusive, cooled very rapidly to temperatures lower than 110°C ($55 \pm 55^\circ\text{C}$) and stayed at these temperatures until ~25 Ma when it began to heat up. The expected model suggests that sample SM15-21 reached a maximum (post emplacement) temperature of $75 \pm 15^\circ\text{C}$ between 10 and 8 Ma, which corresponds to a mean heating rate of $1.3^\circ\text{C}/\text{Myr}$. Subsequent cooling up to the surface (modeled at $25 \pm 5^\circ\text{C}$) since 9 ± 1 Ma is modeled at a rate of $5.3 \pm 2.5^\circ\text{C}/\text{Myr}$. We note that sample SM15-07+09 has a younger apatite fission-track age (22.6 ± 2.8 Ma) than the others and that its expected model suggests a point of inflection of the thermal history at higher temperature than the two other samples, which is compatible with the thermobarometry results that suggest it crystallized deeper than the other samples.

6. Discussion

6.1. Evaluation of the Low Temperature Data

The apatite fission-track central ages of samples SM15-18 and SM15-21 have large uncertainties and within these uncertainties, they are equivalent or older than the zircon fission-track central ages on the same samples

(Table 2). This could be due to the effect of a long residence time in the partial annealing zone of the apatite fission-track system. Alternatively, or additionally, this could be due to the presence in the apatites of both samples of many defects that were difficult to differentiate from spontaneous tracks. This issue lowered significantly the number of countable grains and may have affected the measured ages, despite our best efforts to count only grains with no or few defects. Moreover, in the case of SM15-21, uranium concentration in the analyzed apatites is low (average < 7 ppm, Table 2), which results in a low spontaneous track-density and a large age uncertainty.

Apatite (U-Th)/He ages within single sample show variations that exceed the analytical error. This age dispersion may have different explanations (e.g., Fitzgerald et al., 2006; Shuster et al., 2006). (a) Zoning of U and Th in the grains may influence ages, but the numerous etched apatites used for fission-track analyses did not show such a feature. (b) Excess ^4He stemming from the presence of inclusion(s) or from implantation by neighboring radioactive minerals may also result in an age variability. However, except for one outlier, there is a good positive correlation between the effective uranium (eU) and the corrected He content, thus suggesting that there is no ^4He in excess (Figure 10a). (c) High radiation damage in apatites may affect their He retention (Flowers et al., 2007, 2009; Gautheron et al., 2009; Green et al., 2006; Shuster et al., 2006; Shuster & Farley, 2009), however there is no evident correlation between individual apatite (U-Th)/He ages and eU for the analyzed samples (Figure 10b), which suggests there is no control of radiation damage on He diffusivity. (d) Grain size may also influence diffusion (Farley, 2000; Wolf et al., 1998), larger grains yielding older ages. However, this factor does not seem to affect our data since there is no apparent correlation between the spherical radius (R_s) of the apatite and their individual ages (Figure 10c). (e) Variable composition of apatite also implies differences in the He diffusion kinetics, especially in slow cooling rocks. When the cooling rate is low (<3°C/Myr), apatite (U-Th)/He single-grain ages show a larger dispersion than for higher cooling rates (Fitzgerald et al., 2006). In our study it thus seems that variable apatite composition and long residence time in the partial retention zone of helium in apatite are the factors playing the most important role in the age dispersion. Hence, our QTQt models (in which dispersion due to slow cooling rate is accounted for) show very slow cooling rates (<5°C/Myr), samples staying in the apatite He partial retention zone for at least 8 Ma (sample SM15-07+09) and likely more than 20 Ma for samples SM15-18 and SM15-21.

6.2. Tectono-Thermal Evolution of St. Martin Island

6.2.1. Plutonic Emplacement Conditions

After plutonic emplacement, thermal relaxation of the crust down to temperatures equivalent to those existing before the intrusion occurs in two stages (Fu et al., 2010). First, the crystallization of the intrusion is accompanied by very high cooling rates of the pluton and heating of the host rocks by conduction. The intensity and duration of this cooling is mainly controlled by the emplacement depth and size of the intrusive body. Second, the pluton and its country rocks cool to the pre-intrusion geothermal gradient. During the second stage, the cooling rate is much slower than during the first and it decreases with time as a function of the depth and size of the intrusive body and of the background exhumation rate (Fu et al., 2010). Subsequently, cooling mainly depends on the geothermal gradient variations and exhumation rate, which are controlled by surface processes (sedimentation, erosion, surface temperature) and tectonic processes affecting the crust (faulting, regional uplift, plate kinematics change).

Our new zircon U-Pb ages and thermobarometry data refine the timing and depth of emplacement of the St. Martin granodiorite that intrudes a middle to upper Eocene submarine volcano-sedimentary sequence (Andréieff et al., 1988). We show that the granodiorite emplaced at least over a ~2.1 Myr period between 6.2 and 3.5 km-depth. In particular, sample SM15-09 yielded brown (Ti-rich) and green (Ti-poor) hornblendes for which we calculated crystallization depths of 6.2 and 4.4 km, respectively. It is thus likely that the magma was ascending while partially crystallizing.

The thermobarometry and geo-thermochronology data for the northern pluton are in agreement: the younger the zircon U-Pb age, the higher the crystallization depth given by Al-in-hornblende thermobarometry, and the higher the temperature for the inflection of the time-temperature path towards slower cooling rates. These observations suggest that volcanic activity continued while magma (pluton and satellite sills) was emplaced at depth, under an Oligocene volcano-sedimentary sequence, which is now eroded. These deposits may have been only preserved in St. Martin at Baie Rouge, in the hanging wall of the Bluff Fault, where non-metamorphic pyroclastic depos-

its, recently dated to the Oligocene by Cornée et al. (2021), crop out below the Miocene deposits (Figure 2). Similarly, on St. Barthélemy, surface lava flows dated at ~ 24 Ma ($^{40}\text{Ar}/^{39}\text{Ar}$ on hornblende) are observed unconformably overlying upper Eocene carbonate platform deposits (Cornée et al., 2020; Legendre et al., 2018). Thermobarometrical data on the granodiorite also implies that the lower-middle Eocene volcano-sedimentary deposits intruded by the granodiorite were buried at a depth of ~ 3.5 – 4.5 km, while the geothermal gradient was likely high (higher than $45^\circ\text{C}/\text{km}$). The sub-greenschists facies metamorphism affecting this series is rather due to arc thickening during volcanic activity or to hydrothermal processes rather than to contact metamorphism as previously inferred (Dagain et al., 1989; Davidson et al., 1993). Our field observations confirm that contact metamorphism only affected several centimeters to meters at maximum of country rocks and is thus very limited. Consequently, we interpret our newly dated andesite (SM16-25) and the one of Nagle et al. (1976) as sills intruding the Eocene series connected to the Oligocene pluton (Figure 4) and not as an Eocene lava flow reset by contact metamorphism as described by Andreïeff et al. (1988).

6.2.2. Montserrat Island: A Good Present-Day Analog of St. Martin During the Oligocene

The lithologies cropping out in St. Martin as well as the emplacement depths we calculated from thermobarometry are similar to the present-day structure of the active Soufriere Hills Volcano of Montserrat. The seismic velocity model obtained for this active volcanic island by refraction and reflection tomography (Paulatto et al., 2010) reveals the presence of (a) a “basement” layer that has been proposed to correspond to plutonic and hypabyssal rocks of a previous volcanic arc, (b) a surficial sediment layer likely made of calcareous and volcanoclastic rocks and located offshore of Montserrat island, which could be an analog of the Eocene volcano-sedimentary series cropping out in St. Martin, and (c) a pile of andesite lava domes and intrusions under the volcanic centers, which are similar to both the upper Eocene lava flows of St. Martin and the Oligocene intrusion. A refined model of the magmatic structures under the Montserrat active volcano indicates that the magmatic chamber has a small radius of 1–2 km and extends at least from 5.5 to 7.5 km-depth (Paulatto et al., 2012). The Oligocene granodiorite and the Eocene volcanosedimentary series outcropping in St. Martin island, are thus good exhumed analogs of the present-day shallow intrusions of the active arc.

6.2.3. Exhumation History of St. Martin Island Rocks

Together, our results of thermobarometry and thermal history modeling show that less than 3 Myrs after the end of known magmatic activity in St. Martin, around ~ 24 Ma, samples SM15-21 and SM15-18, which emplaced at ~ 4 km-depth were at temperatures lower than 100°C , the expected model being at temperatures of ~ 60 and $\sim 40^\circ\text{C}$, respectively. Considering that there was no exhumation between the emplacement of the pluton at ~ 4 – 5 km-depth and 24 Ma, we should contemplate that the geothermal gradient decreased drastically by 24 Ma to low values inferior to $11^\circ\text{C}/\text{km}$ in the upper 5 km of the crust. More likely, emplacement was accompanied by rapid exhumation as suggested by the numerous syn-emplacement normal faults (Figure 7). This exhumation event might be associated to the opening of the Anegada rift. Indeed, cooling ages of ~ 20 Ma associated to the rifting were recently reported in Puerto Rico and Virgin Islands (Román et al., 2020).

Rapid exhumation of the St. Martin granodiorite likely stopped around ~ 24 Ma as suggested by the beginning of slow cooling of sample SM15-07+09, the preservation at constant temperature of samples SM15-18 (near the surface) and the beginning of reheating and burial of sample SM15-21 (Figure 9). This period of moderate heating (expected model suggests a $\sim 20^\circ\text{C}$ heating) may be associated to the onset of the deposition of the Miocene platform deposits in this area, which thus would have been less than 700 meters thick (considering a $30^\circ\text{C}/\text{km}$ geothermal gradient). However, our thermal models are not very well constrained at such low temperatures (Figure 9).

Yet, the description of the Miocene deposits allows defining a transgressive episode between ~ 21 Ma and the Tortonian, which was accompanied by slow subsidence that allowed accumulating at least 50 m of sediments. This transgression is interrupted by a period of uplift, likely associated to syn-late Burdigalian to early Langhian faulting (between 18 and 15 Ma), which led to depositional gaps in St. Martin island and mass wastings deposits in Tintamarre island (Cornée et al., 2021). At *ca.* 8.2 Ma, St. Martin deposits exhibit a regressive trend, which leads to emersion at ~ 4 Ma. Miocene marine deposits are now observed at a maximum elevation of ~ 60 m above sea level, suggesting that slow surface uplift has been occurring since 8.2 Ma. This is constrained by the apatite (U-Th)/He age of sample SM15-21, which suggests cooling from 2–1 km depth since ~ 8.5 Ma (Figure 9). We suggest that this period of surface uplift is accompanied by post-Zanclean normal faulting (Figure 7).

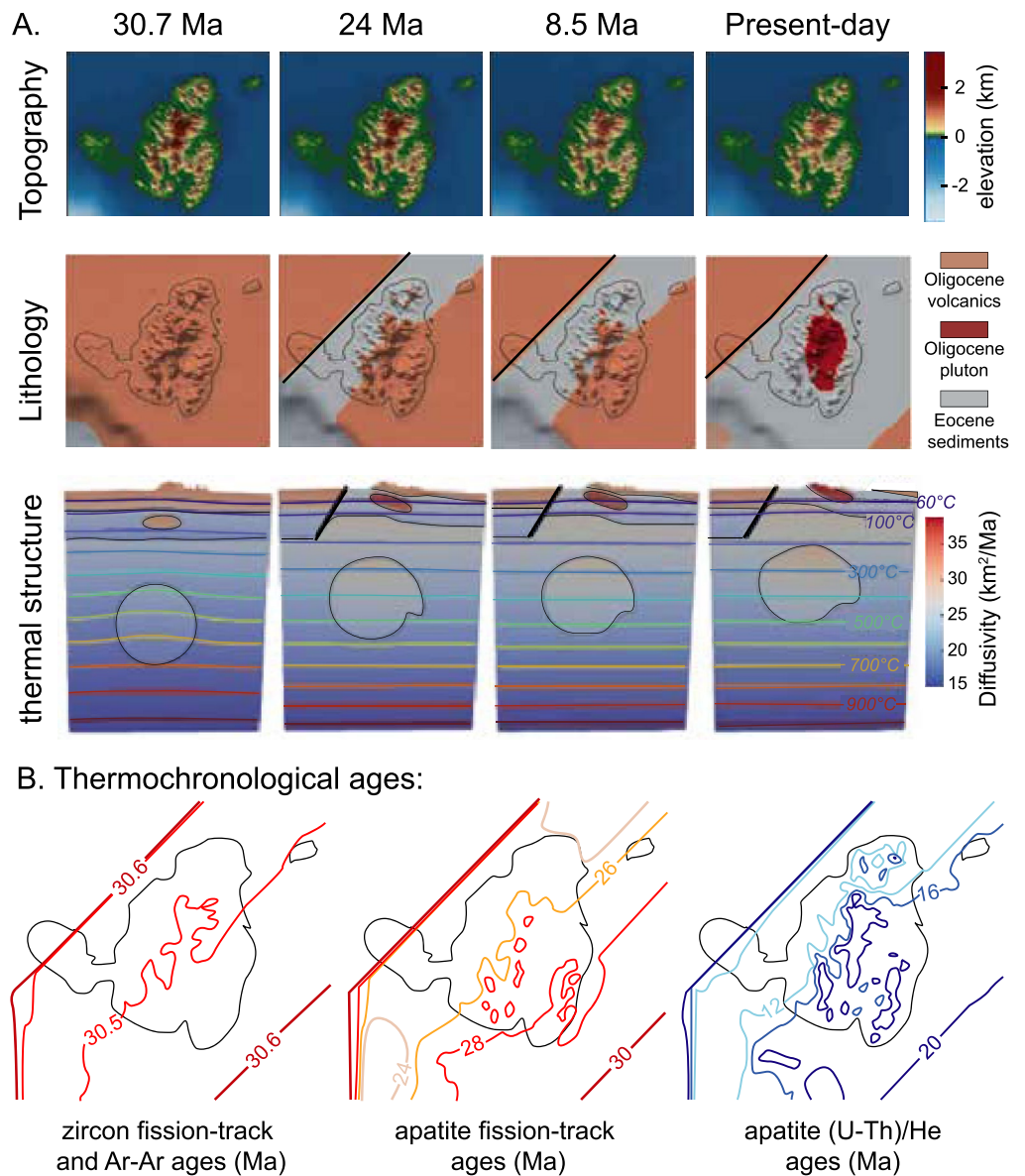


Figure 11. Results of forward Pecube modeling. (a) For each main time steps, we present the topography, the expected outcropping lithology (initial setting is described in Figure 3) and the thermal structure of the crust. (b) Predicted thermochronological ages maps.

6.2.4. Tectono-Thermal Modeling

Our new tectonic data set indicates that since the Eocene, the obtained paleostress tensors are consistent with a NE–SW directed extension responsible for the development or the reactivation of N45° structures such as the Bluff fault that tilted the whole island toward the west. It is to note that the post-intrusion radial stress field giving a σ_3 oriented NW–SE might have undergone switch between σ_3 and σ_2 axis (as their magnitudes are very similar). The switch from radial to pure extension might reflect regional geodynamical changes in the boundary conditions along the Lesser Antilles trench as pointed out by Legendre et al. (2018). Interestingly, a switch of σ_1 from vertical to horizontal has been demonstrated during magma intrusion (Vigneresse et al., 1999), within a radial extensional stress field this switch results in transtensive condition during pluton intrusion. Moreover, thermal history modeling along with thermobarometry and geological constraints suggest that most of the 4–5 km of total exhumation must have occurred before 24 Ma (Figure 9). Considering these results and the platform

deposits of Miocene to Zanclean age, we propose a four-step uplift/subsidence scenario for the St. Martin island. According to our scenario, uplift and subsidence alternated through time, hot magmas intruded in the Oligocene, and the geothermal gradient in the upper crust varied. This impedes to derive exhumation rates from the cooling history obtained using QTQt inverse modeling. Nevertheless, Pecube forward modeling (Braun, 2003) allows reconstructing this evolution (Figure 11) and testing if a given tectonic scenario is able to reproduce the obtained structure and thermochronological ages.

Considering the constraints given by our thermobarometry, thermal history and sedimentary study, we used rock uplift values of 0.6 km/Myr rate between 30.7 and 24 Ma, rock subsidence at a rate of 0.01 km/Myr between 24 Ma and Burdigalian (~16 Ma), uplift at a rate of 0.01 km/Myr between 16 and ~15 Ma, followed by subsidence until 8.5 Ma at a rate of 0.01 km/Myr and uplift at a 0.25 km/Myr rate since then (Figure 3).

Our model predicts that at 24 Ma, 2.7 Myr after the end of magmatic heating, the 200°C isotherm stands at ~6 km below sea level, which corresponds to a ~33°C/km geothermal gradient for the upper crust (Figure 11). At present-day, the modeled crust is colder as the 200°C isotherm is at ~8.7 km below sea level, which corresponds to a ~23°C/km geothermal gradient for the upper crust (Figure 11). This variation of the geothermal gradient through time is due to the time needed to dissipate the heat generated by the magmatic emplacement between 30.7 and 26.7 Ma and to the advection of isotherms due to rapid rock uplift during the 30.7–24 Ma period.

Moreover, Pecube forward model allows reconstructing the geological architecture of the island with a monoclinical tilt of the Eocene sedimentary series of 20° towards the SW and a shape of the Oligocene pluton outcropping more or less in the same area as in St. Martin (Figure 11). Oligocene volcanic series that were likely covering the Eocene sediments and which correspond to the volcanic counterparts of the Oligocene St. Martin granodiorite, are in this scenario predicted to be eroded very early in the history of the island along the Bluff fault but preserved in the south-eastern part of the island until the late Miocene. However, some of these deposits may be preserved in the hanging wall of the Bluff fault as observed in Baie Rouge and SW of the island (Figure 11a), mainly offshore, where they are likely covered by Miocene deposits (Terre Basse, Andréieff et al., 1988; Dagain et al., 1989). This rapid denudation and tilting during the first time-step is due to the uplift rate we imposed on the Bluff fault during magmatic emplacement (30.7–26.7 Ma) and the following 2.7 Myr (until 24 Ma). This scenario allows explaining the obtained apatite fission-track ages older than 24 Ma as well as the ~18 Ma (U-Th)/He apatite ages from sample SM15-18 (Figure 11b). Younger apatite fission-track age of sample SM15-07+09 (22.6 ± 2.8 Ma) might be explained by its higher emplacement depth (ca. 5 km). However, we were not able to reproduce (U-Th)/He apatite ages younger than 10 Ma along the Bluff fault as obtained for samples SM15-07+09 and SM15-21 (~7–8 Ma). This may be due to underestimated rock uplift rate values since 8.5 Ma or to differences between real and modeled topography.

6.3. Regional Implications

Regionally, the emplacement of the St. Martin pluton is contemporaneous with the end of the opening of the Kalinago basin (late Eocene-early Oligocene, Cornée et al., 2021). The pluton emplaced along the eastern shoulder of the Kalinago rift, after 10 Myrs of extension, responsible for localized crustal thinning. From 30.7 to 27 Ma, during the emplacement of the St. Martin Granodiorite, deformation in St. Martin changed from purely extensional along N70° trending faults to transtensional along N20° faults after intrusion. Once the pluton emplaced, radial extension along N45° faults (as the Bluff fault) led to the tilt of the whole island and was accompanied by rapid exhumation. Our Pecube forward modeling shows that a ~0.6 km/Myr exhumation rate during the 30.7 to 24 Ma period is consistent with the obtained zircon U-Pb, $^{40}\text{Ar}/^{39}\text{Ar}$ and fission-track ages. The tilt of the Eocene series is also observed in St. Barthélemy, an island located 30 km SE of St. Martin. However, in St. Martin the Eocene volcanic series dips to the SE whereas in St. Barthélemy it dips to the SSW. It has been proposed that tilting of the Eocene volcanic series is related to a regional-scale deformation event that occurred before the Oligocene (Andréieff et al., 1988; Legendre et al., 2018; Westercamp & Andréieff, 1983). The Bluff fault, responsible for the main vertical motion (and tilting) in St. Martin, trends N45°, parallel to the main crustal faults bounding the V-Shaped basins, and the timing of its activity is similar and postdate the opening of the Anegada Trough (Boucard et al., 2021). Similar N45° trending faults exist in the neighboring island of St. Barthélemy (south of St. Martin, Legendre et al., 2018 and reference therein). However, in Saint-Barthélemy these faults were active earlier and only during the Early Oligocene magmatic event, suggesting that at regional scale, this fault trend

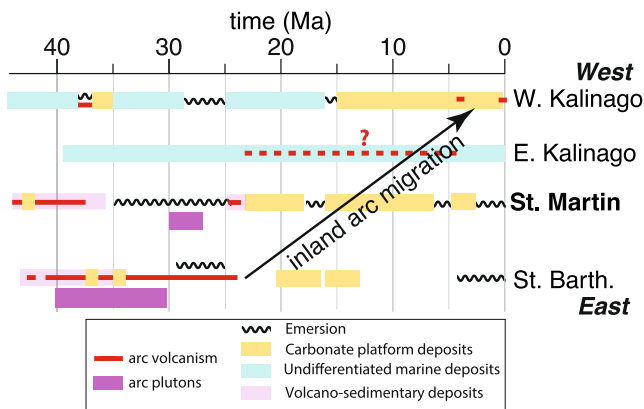


Figure 12. Main regional volcano-sedimentary events since the Eocene in northern Lesser Antilles. Volcano-sedimentary data is adapted from Cornée et al. (2021).

might be an inherited primitive structure potentially reactivated as a function of both far field stress changes and magmatic ascent across the crust.

From *c.a.* 24 Ma to 8 Ma, a syndepositional faulting phase occurred along E–W structures under a radial extensional stress field. These faults controlled the subsidence of the island (at a 0.01 km/Myr rate) and deposition of a carbonate platform. In addition to tectonic control of the subsidence, we propose that when the magmatic activity stopped in the present-day forearc and began to migrate (or jump, Bouysse et al., 1990) towards the west, the crust cooled down as illustrated in Figure 11 and consequently gained in density (or lost its buoyancy), which may have triggered subsidence. Indeed, recent findings (Boucard et al., 2021; Cornée et al., 2021), show that the migration of the Lesser Antilles arc is accompanied by regional drowning of the Anguilla bank from 15 to ~5 Ma. Moreover, we demonstrate that in St. Martin the magmatic emplacement is contemporaneous with extension and exhumation (Figure 12). However, it has to be noted that a short period of surface uplift and emersion occurred between 18 and 15 Ma (Cornée et al., 2021, see Section 6.2.3 and Figure 12).

Since 8 Ma, a last phase of uplift exposed the Mio-Pliocene carbonate deposits in various areas of the Anguilla Bank (St. Martin, St. Barthélemy, Figure 12). This last, purely extensional deformation phase is most probably unrelated to the migration of the volcanic arc. An exhumation rate of 0.25 km/Myr during this period is compatible with the observed geometry of the island and the majority of the obtained apatite (U-Th)/He ages (Figure 11). The region of the Anguilla bank from which St. Martin and St. Barthélemy islands stand out consists in a Paleocene to Eocene basin, where interbedded volcano-sedimentary deposits, carbonates and lavas were deposited (Figure 12, Bouysse & Westercamp, 1990; Bouysse et al., 1990; Cornée et al., 2020; Legendre et al., 2018; Philippon et al., 2020). After a regional event of inversion and emersion during late Eocene-Early Oligocene (Cornée et al., 2020; Philippon et al., 2020), subduction-related plutonic bodies intruded the Paleocene to Eocene volcano-sedimentary deposits (Figure 12). Exhumation rates provided in this study for the Anguilla bank are in the same order of magnitude with the ones recently obtained by (U-Th)/He for the Virgin Island (Román et al., 2020), which are located north of the Anegada Trough. All together, these data suggest a southward migration of the deformation associated with the opening of the Anegada Trough: with a larger amount of exhumation, at high rates, leading to the exposure of large plutonic bodies in the Virgin Island between 24 and 21 Ma, and moderate exhumation (only a few tens of meter over the last 5 Ma in Anguilla and St. Martin) south of the Anegada Trough along faults that trend parallel to the trough. As suggested by various recent studies (Boucard et al., 2021; Legendre et al., 2018; Philippon et al., 2020), the observed regional segmentation of the forearc in rigid micro blocks bounded by NE–SW faults might reflect the accommodation of progressive trench curvature during the last 30 Myrs. With this study we constrain the rate of exhumation affecting the hanging wall of such NE–SW trending faults at 2.5 mm/yr.

Moreover, what causes the arc migration away from the trench is still discussed. It was first proposed that slab break-off followed by a change of the slab dip might have caused arc retreat (Bouysse et al., 1990). However, neither the geochemistry of Lesser Antilles magmas nor tomography studies show evidence of a slab break-off event (Westercamp & Andréieff, 1983; van Benthem et al., 2013). South of the Anguilla bank, in Guadeloupe, tectonic erosion has been proposed as a possible mechanism to explain extension and arc retreat during the last 14 Myrs (De Min et al., 2015), which is consistent with the continuous drowning of the forearc in this region. North of Guadeloupe, at the latitude of the Anguilla bank, the northern part of the Lesser Antilles forearc records drowning and uplift with a frequency of several Myrs and an amplitude of hundreds of meters (this study, Cornée et al., 2020, 2021). Our results suggest that surface uplift has been contemporaneous with intrusion and extension. In this context, the surface uplift related to pluton emplacement (a buoyant and hot feature emplaced in a relatively colder crust) is directly function of its volume, whereas extensional tectonics thin the crust and trigger surface subsidence. Thus, the balance between buoyant and tectonic forces may not be the only mechanism to explain the present-day emersion of the northern Lesser Antilles forearc. These important vertical movements, which are not observed in the southern part of the arc, may reflect coupling variations along the subduction interface. These mechanical changes could have been triggered by punctual episodes of tectonic erosion that might also have been

responsible for the westward migration of the arc during the Oligocene (Boucard et al., 2021). However, geochemical and geochronological constraints evidencing, or not, these episodes of tectonic erosion are still lacking.

7. Conclusions

Thermobarometrical data obtained on the St. Martin granodiorite reveal that this Oligocene pluton outcropping in the present-day Lesser Antilles forearc emplaced and crystallized at 4–5 km depth. Combined structural, stratigraphic and thermochronologic data suggest that this shallow volcanic-arc pluton had a four-step history, which we reconstructed using Pecube forward modeling. The proposed model convincingly reproduces both the observed present-day geometry of St. Martin island and the obtained thermochronological ages. It consists in an initial setting similar to the present-day crustal structure of the Monserrat island, located in the active volcanic arc, and consider the following four-step history:

1. plutonic intrusion between 30 and 27 Ma along N–S transtensive structures;
2. rapid exhumation (0.6 mm/yr) controlled by N45° trending structures contemporaneous with rapid post-emplacment cooling between 27 and 24 Ma;
3. only minor syn-sedimentary deformation occurred along E–W trending faults between 24 and 8.5 Ma and;
4. slow exhumation after 8.5 Ma and uplift of carbonate platforms along mainly N45° trending faults.

At the regional scale this evolutionary scenario is consistent with recent data from the Virgin Islands and suggests a southward migration of the deformation associated with the opening of N40° trending structures that dissect the Lesser Antilles forearc along the Anegada Trough and the V-shaped basins. We propose that the development of carbonate platforms is allowed by the slow drowning of the Anguilla bank (subsidence rate of ~0.01 mm/yr), which may be associated to the westward migration of the arc and subsequent cooling of the crust. Our results give constraints on the exhumation history associated to the NE–SW trending faults that accommodate the progressive curvature of the northern Lesser Antilles subduction trench for the last 30 Myrs, generating deep basins perpendicular to the trench.

Data Availability Statement

Figure S1 and Table S1 in Supporting Information S1 and IGSN identifiers of the samples (Table S2 in Supporting Information S1) as well as QTQt and Pecube input files are included in the supplementary materials uploaded along with this manuscript. The geochronological data set is accessible publicly in the *Geochron* data repository (http://www.geochron.org/dataset/html/geochron_dataset_2021_05_12_hMKWo).

Acknowledgments

We thank M. Balvay and A. Iemmo for their valuable help within the ISTerre fission-track laboratory and the Geoscience Montpellier ⁴⁰Ar/³⁹Ar dating facilities, respectively. Manuscript was kindly proofread by E. González Becuar and G. Solano García. M.N. warmly thanks J. Braun for his precious advices regarding Pecube modeling. This work was supported by the INSU TelluS-SYSTER Oblisub (grant call 2017) and the GAARAnti project (ANR-17-CE31-0009). Aurelie Germa, an anonymous reviewer and Associate Editor Giuditta Fellin are thanked for their fair and constructive reviews.

References

- Ague, J. J., & Brimhall, G. H. (1988). Regional variations in bulk chemistry, mineralogy, and the compositions of mafic and accessory minerals in the batholiths of California. *Geological Society of America Bulletin*, 100(6), 891–911. [https://doi.org/10.1130/0016-7606\(1988\)100<0891:r vibcm>2.3.co;2](https://doi.org/10.1130/0016-7606(1988)100<0891:r vibcm>2.3.co;2)
- Anderson, J. L., Barth, A. P., & Young, E. D. (1988). Mid-crustal Cretaceous roots of Cordilleran metamorphic core complexes. *Geology*, 16(4), 366–369. [https://doi.org/10.1130/0091-7613\(1988\)016<0366:mccroc>2.3.co;2](https://doi.org/10.1130/0091-7613(1988)016<0366:mccroc>2.3.co;2)
- Andréieff, P., Baubron, J. C., & Westercamp, D. (1988). Histoire géologique de la Martinique (Petites Antilles): Biostratigraphie (foraminifères), radiochronologie (potassium–argon), évolution volcano-structurale. *Géologie de la France*, 2(3), 39–70.
- Angelier, J. (1979). Determination of the mean principal directions of stresses for a given fault population. *Tectonophysics*, 56(7), 17–26. [https://doi.org/10.1016/0040-1951\(79\)90081-7](https://doi.org/10.1016/0040-1951(79)90081-7)
- Angelier, J., & Mechler, P. (1977). Sur une méthode graphique de recherche des contraintes principales également utilisable en tectonique et en séismologie: La méthode des dièdres droits. *Bulletin de la Societe Geologique de France*, 7(XIX n°6), 1309–1318. <https://doi.org/10.2113/gssgfbull.s7-xix.6.1309>
- Bernet, M., Brandon, M. T., Garver, J. I., & Molitor, B. R. (2004). Fundamentals of detrital zircon fission-track analysis for provenance and exhumation study with examples from the European Alps. In M. Bernet, & C. Spiegel (Eds.), *Detrital thermochronology–Provenance analysis, exhumation, and landscape evolution of mountain belts* (Vol. 378, pp. 25–36). Special Papers Geological Society of America. <https://doi.org/10.1130/0-8137-2378-7.25>
- Bonneton, J. R., & Vila, J. M. (1983). Données géologiques nouvelles à l'île de Saint-Martin (Petites Antilles). *Bulletin de la Societe Geologique de France*, 25(6), 867–871. <https://doi.org/10.2113/gssgfbull.s7-xxv.6.867>
- Bosch, D., Garrido, C. J., Bruguier, O., Dhuime, B., Bodinier, J. L., Padron-Navarta, J. A., & Galland, B. (2011). Building an island-arc crustal section: Time constraints from a LA-ICP-MS zircon study. *Earth and Planetary Science Letters*, 309(3–4), 268–279. <https://doi.org/10.1016/j.epsl.2011.07.016>

- Boucard, M., Marcaillou, B., Lebrun, J. F., Laurencin, M., Klingelhofer, F., Laigle, M., et al. (2021). Paleogene V-Shaped Basins and Neogene Subsidence of the Northern Lesser Antilles Forearc. *Tectonics*, *40*(3), e2020TC006524. <https://doi.org/10.1029/2020tc006524>
- Bouysse, P., & Westercamp, D. (1990). Subduction of Atlantic aseismic ridges and Late Cenozoic evolution of the Lesser Antilles island-arc. *Tectonophysics*, *175*(4), 349–380. [https://doi.org/10.1016/0040-1951\(90\)90180-g](https://doi.org/10.1016/0040-1951(90)90180-g)
- Bouysse, P., Westercamp, D., & Andréieff, P. (1990). The Lesser Antilles island arc. In J. C. Moore, et al. (Eds.), *Proceedings of the ocean drilling program, scientific results* (Vol. 110, pp. 29–44). Ocean Drilling Program. <https://doi.org/10.2973/odp.proc.sr.110.166.1990>
- Brandon, M. T., Roden-Tice, M. K., & Garver, J. I. (1998). Late Cenozoic exhumation of the Cascadia accretionary wedge in the Olympic Mountains, northwest Washington State. *Geological Society of America Bulletin*, *110*(8), 985–1009. [https://doi.org/10.1130/0016-7606\(1998\)110<0985:lceotc>2.3.co;2](https://doi.org/10.1130/0016-7606(1998)110<0985:lceotc>2.3.co;2)
- Braun, J. (2003). Pecube: A new finite element code to solve the heat transport equation in three dimensions in the Earth's crust including the effects of a time-varying, finite amplitude surface topography. *Computers & Geosciences*, *29*(6), 787–794. [https://doi.org/10.1016/s0098-3004\(03\)00052-9](https://doi.org/10.1016/s0098-3004(03)00052-9)
- Braun, J., Van Der Beek, P., & Batt, G. (2006). *Quantitative thermochronology: Numerical methods for the interpretation of thermochronological data*. Cambridge University Press.
- Briden, J. C., Rex, D. C., Faller, A. M., & Tomblin, J. F. (1979). K-Ar geochronology and palaeomagnetism of volcanic rocks in the Lesser Antilles island arc. *Philosophical Transactions of the Royal Society of London-Series A: Mathematical and Physical Sciences*, *291*(1383), 485–528.
- Cailleau, B., & Oncken, O. (2008). Past forearc deformation in Nicaragua and coupling at the megathrust interface: Evidence for subduction retreat? *Geochemistry, Geophysics, Geosystems*, *9*(3), Q03016. <https://doi.org/10.1029/2007gc001754>
- Carlson, W. D., Donelick, R. A., & Ketcham, R. A. (1999). Variability of apatite fission-track annealing kinetics: I. Experimental results. *American Mineralogist*, *84*, 1213–1223. <https://doi.org/10.2138/am-1999-0901>
- Chaytor, J. D., & ten Brink, U. S. (2015). Event sedimentation in low-latitude deep-water carbonate basins, A negada passage, northeast Caribbean. *Basin Research*, *27*(3), 310–335. <https://doi.org/10.1111/bre.12076>
- Christman, R. A. (1953). Geology of St. Bartholomew, St. Martin, and Anguilla, Lesser Antilles. *Geological Society of America Bulletin*, *64*(1), 65–96. [https://doi.org/10.1130/0016-7606\(1953\)64\[85:gosbsm\]2.0.co;2](https://doi.org/10.1130/0016-7606(1953)64[85:gosbsm]2.0.co;2)
- Clift, P., & Vannucchi, P. (2004). Controls on tectonic accretion versus erosion in subduction zones: Implications for the origin and recycling of the continental crust. *Reviews of Geophysics*, *42*(2), RG2001. <https://doi.org/10.1029/2003rg000127>
- Cornée, J.-J., Boudagher-Fadel, M., Philippon, M., Léticée, J.-L., Legendre, L., Moincent, G., et al. (2020). Paleogene carbonate systems of Saint Barthélemy, Lesser Antilles: Stratigraphy and general organization. *Newsletters on Stratigraphy*, *53*(4), 461–478.
- Cornée, J.-J., Münch, P., Philippon, M., Boudagher-Fadel, M., Quillévére, F., Melinte-Dobrinescu, M., et al. (2021). Lost islands in the northern Lesser Antilles: Possible milestones in the Cenozoic dispersal of terrestrial organisms between South-America and the Greater Antilles. *Earth-Science Reviews*, *217*, 10361.
- Corrigan, J., Mann, P., & Ingle, J. C., Jr (1990). Forearc response to subduction of the Cocos ridge, Panama-Costa Rica. *Geological Society of America Bulletin*, *102*(5), 628–652. [https://doi.org/10.1130/0016-7606\(1990\)102<0628:frtsot>2.3.co;2](https://doi.org/10.1130/0016-7606(1990)102<0628:frtsot>2.3.co;2)
- Dagain, J., Andréieff, P., Westercamp, D., Bouysse, P., & Garrabe, F. (1989). *Notice et carte géologique de Saint-Martin 1/50 000, Antilles Françaises, Département de la Guadeloupe, éd (Vol. 3)*. BRGM.
- Davidson, J. P., Boghossian, N. D., & Wilson, M. (1993). The geochemistry of the igneous rock suite of St Martin, northern Lesser Antilles. *Journal of Petrology*, *34*(5), 839–866. <https://doi.org/10.1093/ptrology/34.5.839>
- Defant, M. J., Sherman, S., Maury, R. C., Bellon, H., De Boer, J., Davidson, J., & Kepezhinskis, P. (2001). The geology, petrology, and petrogenesis of Saba Island, Lesser Antilles. *Journal of Volcanology and Geothermal Research*, *107*(1–3), 87–111. [https://doi.org/10.1016/s0377-0273\(00\)00268-7](https://doi.org/10.1016/s0377-0273(00)00268-7)
- De Grave, J., Zhimulev, F. I., Glorie, S., Kuznetsov, G. V., Evans, N., Vanhaecke, F., & McInnes, B. (2016). Late Palaeogene emplacement and late Neogene–Quaternary exhumation of the Kuril island-arc root (Kunashir island) constrained by multi-method thermochronometry. *Geoscience Frontiers*, *7*(2), 211–220. <https://doi.org/10.1016/j.gsf.2015.05.002>
- Delvaux, D., Moëys, R., Stapel, G., Melnikov, A., & Ermikov, V. (1995). Palaeostress reconstructions and geodynamics of the Baikal region, Central Asia, Part I. Palaeozoic and Mesozoic pre-rift evolution. *Tectonophysics*, *252*(1–4), 61–101. [https://doi.org/10.1016/0040-1951\(95\)00090-9](https://doi.org/10.1016/0040-1951(95)00090-9)
- Delvaux, D., & Sperner, B. (2003). New aspects of tectonic stress inversion with reference to the TENSOR program. *Geological Society of London, Special Publications*, *212*(1), 75–100. <https://doi.org/10.1144/gsl.sp.2003.212.01.06>
- De Min, L., Lebrun, J. F., Cornée, J. J., Münch, P., Léticée, J. L., Quillévére, F., et al. (2015). Tectonic and sedimentary architecture of the Karukéra spur: A record of the Lesser Antilles fore-arc deformations since the Neogene. *Marine Geology*, *363*, 15–37. <https://doi.org/10.1016/j.margeo.2015.02.007>
- de Saint-Blanquat, M., Habert, G., Horsman, E., Morgan, S. S., Tikoff, B., Launeau, P., & Gleizes, G. (2006). Mechanisms and duration of non-tectonically assisted magma emplacement in the upper crust: The Black Mesa pluton, Henry Mountains, Utah. *Tectonophysics*, *428*(1–4), 1–31. <https://doi.org/10.1016/j.tecto.2006.07.014>
- Dobrovine, P. V., Steinberger, B., & Torsvik, T. H. (2012). Absolute plate motions in a reference frame defined by moving hot spots in the Pacific, Atlantic, and Indian oceans. *Journal of Geophysical Research: Solid Earth*, *117*(B9), B09101. <https://doi.org/10.1029/2011JB009072>
- Dumitru, T. A. (1993). A new computer-automated microscope stage system for fission-track analysis. *Nuclear Tracks and Radiation Measurements*, *21*(4), 575–580. [https://doi.org/10.1016/1359-0189\(93\)90198-1](https://doi.org/10.1016/1359-0189(93)90198-1)
- Eppelbaum, L., Kutasov, I., & Pilchin, A. (2014). Thermal properties of rocks and density of fluids. In *Applied geothermics* (pp. 99–149). Springer. https://doi.org/10.1007/978-3-642-34023-9_2
- Espurt, N., Baby, P., Brusset, S., Roddaz, M., Hermoza, W., Regard, V., et al. (2007). How does the Nazca Ridge subduction influence the modern Amazonian foreland basin? *Geology*, *35*(6), 515–518. <https://doi.org/10.1130/g23237a.1>
- Farley, K. A. (2000). Helium diffusion from apatite: General behavior as illustrated by Durango fluorapatite. *Journal of Geophysical Research: Solid Earth*, *105*(B2), 2903–2914. <https://doi.org/10.1029/1999jb900348>
- Favier, A., Lardeaux, J.-M., Legendre, L., Verati, C., Philippon, M., Corsini, M., et al. (2019). Tectono-metamorphic evolution of shallow crustal levels within active volcanic arcs. Insights from the exhumed Basal Complex of Basse-Terre (Guadeloupe, French West Indies). *Bulletin de la Société Géologique de France*, *190*(1). <https://doi.org/10.1051/bsgf/2019011>
- Fitzgerald, P. G., Baldwin, S. L., Webb, L. E., & O'Sullivan, P. B. (2006). Interpretation of (U–Th)/He single grain ages from slowly cooled crustal terranes: A case study from the Transantarctic Mountains of southern Victoria Land. *Chemical Geology*, *225*(1–2), 91–120. <https://doi.org/10.1016/j.chemgeo.2005.09.001>
- Fleischer, R. L., Price, P. B., & Walker, R. M. (1964). Fission track ages of zircons. *Geophysical Research*, *69*, 4885–4888. <https://doi.org/10.1029/jz069i022p04885>

- Flowers, R. M., Bowring, S. A., Tulloch, A. J., & Klepeis, K. A. (2005). Tempo of burial and exhumation within the deep roots of a magmatic arc, Fiordland, New Zealand. *Geology*, 33(1), 17–20. <https://doi.org/10.1130/g21010.1>
- Flowers, R. M., Ketcham, R. A., Shuster, D., & Farley, K. A. (2009). Apatite (U–Th)/He thermochronology using a radiation damage accumulation and annealing model. *Geochimica et Cosmochimica Acta*, 73, 2347–2365. <https://doi.org/10.1016/j.gca.2009.01.015>
- Flowers, R. M., Shuster, D., Wernicke, B., & Farley, K. A. (2007). Radiation damage control on apatite (U–Th)/He dates from the Grand Canyon region, Colorado Plateau. *Geology*, 35, 447–450. <https://doi.org/10.1130/g23471a.1>
- Fu, F. Q., McInnes, B. I., Evans, N. J., & Davies, P. J. (2010). Numerical modeling of magmatic–hydrothermal systems constrained by U–Th–Pb–He time–temperature histories. *Journal of Geochemical Exploration*, 106(1–3), 90–109. <https://doi.org/10.1016/j.gexplo.2009.09.001>
- Gallagher, K. (2012). Transdimensional inverse thermal history modeling for quantitative thermochronology. *Journal of Geophysical Research: Solid Earth*, 117(B2), B02408. <https://doi.org/10.1029/2011jb008825>
- Gallagher, K., Charvin, K., Nielsen, S., Sambridge, M., & Stephenson, J. (2009). Markov chain Monte Carlo (MCMC) sampling methods to determine optimal models, model resolution and model choice for Earth Science problems. *Marine and Petroleum Geology*, 26(4), 525–535. <https://doi.org/10.1016/j.marpetgeo.2009.01.003>
- Gautheron, C., Tassan-Got, L., Barbarand, J., & Pagel, M. (2009). Effect of alpha-damage annealing on apatite (U–Th)/He thermochronology. *Chemical Geology*, 266(3–4), 157–170. <https://doi.org/10.1016/j.chemgeo.2009.06.001>
- Geist, E. L., Fisher, M. A., & Scholl, D. W. (1993). Large-scale deformation associated with ridge subduction. *Geophysical Journal International*, 115(2), 344–366. <https://doi.org/10.1111/j.1365-246x.1993.tb01191.x>
- Gelaro, R., McCarty, W., Suárez, M. J., Todling, R., Molod, A., Takacs, L., et al. (2017). The modern-era retrospective analysis for research and applications, version 2 (MERRA-2). *Journal of Climate*, 30(14), 5419–5454. <https://doi.org/10.1175/jcli-d-16-0758.1>
- Green, P. F., Crowhurst, P. V., Duddy, I. R., Jaspén, P., & Holford, S. P. (2006). Conflicting (U–Th)/He and fission track ages in apatite: Enhanced He retention, not annealing behaviour. *Earth and Planetary Science Letters*, 250, 407–427. <https://doi.org/10.1016/j.epsl.2006.08.022>
- Grove, M., & Harrison, T. M. (1996). 40Ar* diffusion in Fe-rich biotite. *American Mineralogist*, 81(7–8), 940–951. <https://doi.org/10.2138/am-1996-7-816>
- Gvirtzman, Z., & Nur, A. (1999). Plate detachment, asthenosphere upwelling, and topography across subduction zones. *Geology*, 27(6), 563–566. [https://doi.org/10.1130/0091-7613\(1999\)027<0563:pdauat>2.3.co;2](https://doi.org/10.1130/0091-7613(1999)027<0563:pdauat>2.3.co;2)
- Habert, G., & de Saint-Blanquat, M. (2004). Rate of construction of the Black Mesa bysmalith, Henry Mountains, Utah. In C. Breitkeuz, & N. Petford (Eds.), *Physical geology of high-level magmatic systems* (Vol. 234, pp. 163–173). Geological Society, London, Special Publication. <https://doi.org/10.1144/gsl.sp.2004.234.01.10>
- Harrison, T. M. (1982). Diffusion of 40 Ar in hornblende. *Contributions to Mineralogy and Petrology*, 78(3), 324–331. <https://doi.org/10.1007/bf00398927>
- Heuret, A., Funicello, F., Faccenna, C., & Lallemand, S. (2007). Plate kinematics, slab shape and back-arc stress: A comparison between laboratory models and current subduction zones. *Earth and Planetary Science Letters*, 256(3–4), 473–483. <https://doi.org/10.1016/j.epsl.2007.02.004>
- Holland, T., & Blundy, J. (1994). Non-ideal interactions in calcic amphiboles and their bearing on amphibole–plagioclase thermometry. *Contributions to Mineralogy and Petrology*, 116(4), 433–447. <https://doi.org/10.1007/bf00310910>
- Jany, I., Scanlon, K. M., & Mauffret, A. (1990). Geological interpretation of combined Seabeam, Gloria and seismic data from Anegada Passage (Virgin Islands, north Caribbean). *Marine Geophysical Researches*, 12(3), 173–196. <https://doi.org/10.1007/BF02266712>
- Jiménez-Díaz, A., Ruiz, J., Pérez-Gussinyé, M., Kirby, J. F., Álvarez-Gómez, J. A., Tejero, R., & Capote, R. (2014). Spatial variations of effective elastic thickness of the lithosphere in Central America and surrounding regions. *Earth and Planetary Science Letters*, 391, 55–66.
- Keppie, D. F., Currie, C. A., & Warren, C. (2009). Subduction erosion modes: Comparing finite element numerical models with the geological record. *Earth and Planetary Science Letters*, 287(1–2), 241–254. <https://doi.org/10.1016/j.epsl.2009.08.009>
- Ketcham, R. A., Carter, A., Donelick, R. A., Barbarand, J., & Hurlford, A. J. (2007). Improved modeling of fission-track annealing in apatite. *American Mineralogist*, 92(5–6), 799–810. <https://doi.org/10.2138/am.2007.2281>
- Ketcham, R. A., Donelick, R. A., & Carlson, W. D. (1999). Variability of apatite fission-track annealing kinetics: III. Extrapolation to geological time scales. *American Mineralogist*, 84(9), 1235–1255. <https://doi.org/10.2138/am-1999-0903>
- Kohn, B., Chung, L., & Gleadow, A. (2019). Fission-track analysis: Field collection, sample preparation and data acquisition. In M. G. Malusà, & P. G. Fitzgerald (Eds.), *Fission-track thermochronology and its application to geology* (pp. 25–48). Springer. https://doi.org/10.1007/978-3-319-89421-8_2
- Kohút, M., & Danišik, M. (2017). Rapid cooling and geospeedometry of granitic rocks exhumation within a volcanic arc: A case study from the Central Slovakian Neovolcanic Field (Western Carpathians). *Island Arc*, 26(5), e12201.
- Koppers, A. A. (2002). ArArCALC—Software for 40Ar/39Ar age calculations. *Computers & Geosciences*, 28(5), 605–619. [https://doi.org/10.1016/s0098-3004\(01\)00095-4](https://doi.org/10.1016/s0098-3004(01)00095-4)
- Lallemand, S. E., Malavieille, J., & Calassou, S. (1992). Effects of oceanic ridge subduction on accretionary wedges: Experimental modeling and marine observations. *Tectonics*, 11(6), 1301–1313. <https://doi.org/10.1029/92tc00637>
- Laurencin, M., Marcaillou, B., Graindorge, D., Klingelhoefer, F., Lallemand, S., Laigle, M., & Lebrun, J.-F. (2017). The polyphased tectonic evolution of the Anegada Passage in the northern Lesser Antilles subduction zone. *Tectonics*, 36, 945–961. <https://doi.org/10.1002/2017TC004511>
- Legendre, L., Philippon, M., Münch, P., Leticée, J.-L., Noury, M., Maincent, G., et al. (2018). Trench bending initiation: Upper plate strain pattern and volcanism. Insights from the Lesser Antilles arc, St. Barthélemy Island, French West Indies. *Tectonics*, 37(9), 2777–2797. <https://doi.org/10.1029/2017tc004921>
- Martinod, J., Gérard, M., Husson, L., & Regard, V. (2020). Widening of the Andes: An interplay between subduction dynamics and crustal wedge tectonics. *Earth-Science Reviews*, 204, 103170. <https://doi.org/10.1016/j.earscirev.2020.103170>
- Martinod, J., Husson, L., Roperch, P., Guillaume, B., & Espurt, N. (2010). Horizontal subduction zones, convergence velocity and the building of the Andes. *Earth and Planetary Science Letters*, 299(3–4), 299–309. <https://doi.org/10.1016/j.epsl.2010.09.010>
- Martinod, J., Regard, V., Letourmy, Y., Henry, H., Hassani, R., Baratchart, S., & Carretier, S. (2016). How do subduction processes contribute to forearc Andean uplift? Insights from numerical models. *Journal of Geodynamics*, 96, 6–18. <https://doi.org/10.1016/j.jog.2015.04.001>
- McDowell, F. W., McIntosh, W. C., & Farley, K. A. (2005). A precise 40Ar–39Ar reference age for the Durango apatite (U–Th)/He and fission-track dating standard. *Chemical Geology*, 214(3–4), 249–263. <https://doi.org/10.1016/j.chemgeo.2004.10.002>
- Merlet, C. (1994). An accurate computer correction program for quantitative electron probe microanalysis. *Microchimica Acta*, 114(1), 363–376. <https://doi.org/10.1007/bf01244563>
- Mutch, E. J. F., Blundy, J. D., Tattitch, B. C., Cooper, F. J., & Brooker, R. A. (2016). An experimental study of amphibole stability in low-pressure granitic magmas and a revised Al-in-hornblende geobarometer. *Contributions to Mineralogy and Petrology*, 171(10), 85. <https://doi.org/10.1007/s00410-016-1298-9>

- Naeser, C. W., & Dodge, F. C. W. (1969). Fission-track ages of accessory minerals from granitic rocks of the central Sierra Nevada Batholith, California. *Geological Society of America Bulletin*, 80, 2201–2212. [https://doi.org/10.1130/0016-7606\(1969\)80\[2201:faoamf\]2.0.co;2](https://doi.org/10.1130/0016-7606(1969)80[2201:faoamf]2.0.co;2)
- Nagle, F., Stipp, J. J., & Fisher, D. E. (1976). K-Ar geochronology of the limestone Caribbees and Martinique, lesser Antilles, West Indies. *Earth and Planetary Science Letters*, 29(2), 401–412. [https://doi.org/10.1016/0012-821x\(76\)90145-x](https://doi.org/10.1016/0012-821x(76)90145-x)
- Noury, M., Philippon, M., Bernet, M., Paquette, J.-L., & Sempere, T. (2017). Geological record of flat slab–induced extension in the southern Peruvian forearc. *Geology*, 45(8), 723–726. <https://doi.org/10.1130/g38990e.1>
- Paulatto, M., Annen, C., Henstock, T. J., Kiddle, E., Minshull, T. A., Sparks, R. S. J., & Voight, B. (2012). Magma chamber properties from integrated seismic tomography and thermal modeling at Montserrat. *Geochemistry, Geophysics, Geosystems*, 13(1), Q01014. <https://doi.org/10.1029/2011gc003892>
- Paulatto, M., Minshull, T. A., Baptie, B., Dean, S., Hammond, J. O., Henstock, T., et al. (2010). Upper crustal structure of an active volcano from refraction/reflection tomography, Montserrat, Lesser Antilles. *Geophysical Journal International*, 180(2), 685–696. <https://doi.org/10.1111/j.1365-246x.2009.04445.x>
- Philippon, M., Cornée, J.-J., Münch, P., Van Hinsbergen, D. J., Boudagher-Fadel, M., Gailler, L., et al. (2020). Eocene intra-plate shortening responsible for the rise of a faunal pathway in the northeastern Caribbean realm. *PLoS One*, 15(10). <https://doi.org/10.1371/journal.pone.0241000>
- Pichot, T., Patriat, M., Westbrook, G. K., Nalpas, T., Gutscher, M. A., Roest, W. R., et al. (2012). The Cenozoic tectonostratigraphic evolution of the Barracuda Ridge and Tiburon Rise, at the western end of the North America–South America plate boundary zone. *Marine Geology*, 303, 154–171. <https://doi.org/10.1016/j.margeo.2012.02.001>
- Renne, P. R., Swisher, C. C., Deino, A. L., Karner, D. B., Owens, T. L., & DePaolo, D. J. (1998). Intercalibration of standards, absolute ages and uncertainties in 40Ar/39Ar dating. *Chemical Geology*, 145(1–2), 117–152. [https://doi.org/10.1016/s0009-2541\(97\)00159-9](https://doi.org/10.1016/s0009-2541(97)00159-9)
- Román, Y. A., Pujols, E. J., Cavosie, A. J., & Stockli, D. F. (2020). Timing and magnitude of progressive exhumation and deformation associated with Eocene arc-continent collision in the NE Caribbean plate. *Geological Society of America Bulletin*, 133(5–6), 1256–1266. <https://doi.org/10.1130/b30941b04p04392>
- Shuster, D., & Farley, K. A. (2009). The influence of artificial radiation damage and thermal annealing on helium diffusion kinetics in apatite. *Geochimica et Cosmochimica Acta*, 73, 183–196. <https://doi.org/10.1016/j.gca.2008.10.013>
- Shuster, D. L., Flowers, R. M., & Farley, K. A. (2006). The influence of natural radiation damage on helium diffusion kinetics in apatite. *Earth and Planetary Science Letters*, 249(3–4), 148–161. <https://doi.org/10.1016/j.epsl.2006.07.028>
- Sisson, V. B., Hollister, L. S., & Onstott, T. C. (1989). Petrologic and age constraints on the origin of a low-pressure/high-temperature metamorphic complex, southern Alaska. *Journal of Geophysical Research: Solid Earth*, 94(B4), 4392–4410. <https://doi.org/10.1029/jb094ib04p04392>
- Tagami, T., Galbraith, R. F., Yamada, R., & Laslett, G. M. (1998). Revised annealing kinetics of fission tracks in zircon and geological implications. In *Advances in fission-track geochronology* (pp. 99–112). Springer. https://doi.org/10.1007/978-94-015-9133-1_8
- Tagami, T., Ito, H., & Nishimura, S. (1990). Thermal annealing characteristics of spontaneous fission tracks in zircon. *Chemical Geology: Isotope Geoscience Section*, 80(2), 159–169. [https://doi.org/10.1016/0168-9622\(90\)90024-7](https://doi.org/10.1016/0168-9622(90)90024-7)
- van Benthem, S., Govers, R., Spakman, W., & Wortel, R. (2013). Tectonic evolution and mantle structure of the Caribbean. *Journal of Geophysical Research: Solid Earth*, 118(6), 3019–3036. <https://doi.org/10.1002/jgrb.50235>
- van Hunen, J., van den Berg, A. P., & Vlaar, N. J. (2000). A thermo-mechanical model of horizontal subduction below an overriding plate. *Earth and Planetary Science Letters*, 182(2), 157–169. [https://doi.org/10.1016/s0012-821x\(00\)00240-5](https://doi.org/10.1016/s0012-821x(00)00240-5)
- van Hunen, J., van den Berg, A. P., & Vlaar, N. J. (2002). The impact of the South-American plate motion and the Nazca Ridge subduction on the flat subduction below South Peru. *Geophysical Research Letters*, 29(14), 35-1–35-4. <https://doi.org/10.1029/2001gl014004>
- Vermeesch, P. (2009). Radialplotter: A java application for fission track, luminescence and other radial plots. *Radiation Measurements*, 44(4), 409–410. <https://doi.org/10.1016/j.radmeas.2009.05.003>
- Vignerresse, J. L., Tikoff, B., & Améglio, L. (1999). Modification of the regional stress field by magma intrusion and formation of tabular granitic plutons. *Tectonophysics*, 302(3–4), 203–224. [https://doi.org/10.1016/S0040-1951\(98\)00285-6](https://doi.org/10.1016/S0040-1951(98)00285-6)
- Vosteen, H. D., & Schellschmidt, R. (2003). Influence of temperature on thermal conductivity, thermal capacity and thermal diffusivity for different types of rock. *Physics and Chemistry of the Earth, Parts A/B/C*, 28(9–11), 499–509. [https://doi.org/10.1016/s1474-7065\(03\)00069-x](https://doi.org/10.1016/s1474-7065(03)00069-x)
- Westercamp, D., & Andréief, P. (1983). Saint-Barthélémy et ses îlets, Antilles Françaises: Géologie et évolution magmato-structurale. *Bulletin de la Société Géologique de France*, 25(6), 873–883. <https://doi.org/10.2113/gssgfbull.s7-xxv.6.873>
- Wiedenbeck, M., Allé, P., Corfu, F., Griffin, W. L., Meier, M., Oberli, F., et al. (1995). Three natural zircon standards for U-Th-Pb, Lu-Hf, trace element and REE analyses. *Geostandards Newsletter*, 19(1), 1–23. <https://doi.org/10.1111/j.1751-908x.1995.tb00147.x>
- Wolf, R. A., Farley, K. A., & Kass, D. M. (1998). Modeling of the temperature sensitivity of the apatite (U–Th)/He thermochronometer. *Chemical Geology*, 148(1), 105–114. [https://doi.org/10.1016/s0009-2541\(98\)00024-2](https://doi.org/10.1016/s0009-2541(98)00024-2)
- Wu, L., Monié, P., Wang, F., Lin, W., Ji, W., Bonno, M., et al. (2016). Cenozoic exhumation history of Sulu terrane: Implications from (U–Th)/He thermochronology. *Tectonophysics*, 672, 1–15. <https://doi.org/10.1016/j.tecto.2016.01.035>
- Yáñez, G., & Cembrano, J. (2004). Role of viscous plate coupling in the late Tertiary Andean tectonics. *Journal of Geophysical Research: Solid Earth*, 109(B2), B02407.